DISSERTATIONES PHYSICAE UNIVERSITATIS TARTUENSIS
48

DISSERTATIONES PHYSICAE UNIVERSITATIS TARTUENSIS
48

OPTICAL INVESTIGATION OF METAL-OXIDE THIN FILMS

VALTER KIISK

TARTU UNIVERSITY
PRESS

CONTENTS

List of abbreviations **7**

List of publications included in the thesis **8**

1 Introduction **9**
1.1 Technological interest in luminescent materials 9
1.2 Group IVa dioxides as wide band gap optical materials 10
1.2.1 TiO_2 (titania) 10
1.2.2 ZrO_2 (zirconia) and HfO_2 (hafnia) 11
1.3 Rare earth ions as optical dopants 13
1.3.1 Introduction 13
1.3.2 Energy level structure 14
1.3.3 Efficiency of luminescence 17
1.3.4 Excitation mechanisms 19
1.4 Aim of the present work 20

2 Preparation of pure and doped metal-oxide materials **21**
2.1 Introduction 21
2.2 Atomic layer deposition 21
2.3 Sol-gel technique 23
2.4 Incorporation of impurities by ion implantation 25

3 Waveguiding in ALD-grown films **29**
3.1 Introduction 29
3.2 Point-source emission within dielectric layers 30
3.3 Resonance near the total internal reflection 33
3.4 Description of samples and experimental details 34
3.5 Results and discussion 35
3.6 Conclusion 38

4 Luminescent materials based on RE-activated metal-oxides **40**
4.1 Introduction 40
4.2 Description of samples and experimental details 40
4.2.1 ALD-grown samples 40
4.2.2 Sol-gel-prepared samples 42
4.2.3 Experimental 42
4.3 Results and discussion 43
4.3.1 Photoluminescence spectra 43
4.3.2 Photoluminescence decay 49
4.3.3 PL excitation spectra 52
4.3.4 Effective cross section of RE excitation 53
4.3.5 Gas sensing behavior 55
4.3.6 Further discussion 57
4.4 Conclusion 59

Summary **60**

Summary in Estonian **62**

Acknowledgements **64**

References **65**

LIST OF ABBREVIATIONS

AFM	atomic force microscopy
ALD	atomic layer deposition
CCD	charge-coupled device
CTR	chemical transport reactions
CT	charge transfer
CTS	charge transfer state
DBR	distributed Bragg reflector
ESR	electron spin resonance
ICCD	intensified charge-coupled device
LED	light emitting diode
PL	photoluminescence
PMT	photomultiplier tube
RE	rare earth
RT	room temperature
RHEED	reflection high-energy electron diffraction
SPM	scanning probe microscopy
STE	self-trapped exciton
UV	ultraviolet (spectral range)
VUV	vacuum ultraviolet (spectral range)
XRD	X-ray diffraction

LIST OF PUBLICATIONS INCLUDED IN THE THESIS

The references will be cited at the end of the corresponding chapter headings.

I V. Kiisk, I. Sildos, O. Sild, and J. Aarik, *Spectral-spatial redistribution of self-trapped excitonic emission in thin anatase films*, in: 19th Congress of the International Commission for Optics (ICO XIX), "Optics for the Quality of Life", Technical Digest (A. Consortini, G. C. Righini, Eds.), Proc. SPIE **4829**, 813–814 (2002).

II V. Kiisk, I. Sildos, O. Sild, and J. Aarik, *The influence of a waveguiding structure on the excitonic luminescence of anatase thin films*, Optical Materials **27**, 115–118 (2004).

III S. Lange, I. Sildos, V. Kiisk, and J. Aarik, *Energy transfer in the photoexcitation of Sm^{3+}-implanted TiO_2 thin films*, Mat. Sci. Eng. B **112**, 87–90 (2004).

IV I. Sildos, S. Lange, T. Tätte, V. Kiisk, M. Kirm, and J. Aarik, *Emission of rare earth ions incorporated into metal oxide thin films and fibres*, MRS Proceedings **796**, V3.6 (2004).

V V. Reedo, S. Lange, V. Kiisk, A. Lukner, T. Tätte, and I. Sildos, *Influence of ambient gas on the photoluminescence of sol-gel derived TiO_2:Sm^{3+} films*, in: Optical Materials and Applications (A. Rosental, ed.), Proc. SPIE **5946**, 59460F (2005).

VI V. Kiisk, I. Sildos, S. Lange, V. Reedo, T. Tätte, M. Kirm, and J. Aarik, *Photoluminescence characterization of pure and Sm^{3+}-doped thin metaloxide films*, Appl. Surf. Sci. **247**, 412–417 (2005).

VII S. Lange, I. Sildos, V. Kiisk, J. Aarik, and M. Kirm, *Photoluminescence of RE-doped thin metal oxide films*, phys. stat. sol. (c) **2**, 326–329 (2005).

VIII S. Lange, V. Kiisk, V. Reedo, M. Kirm, J. Aarik, and I. Sildos, *Luminescence of RE-ions in HfO_2 thin films and some possible applications*, Optical Materials **28**, 1238–1242 (2006).

List of publications not directly connected to the subject of this thesis

IX P. Bohacek, N. Senguttuvan, V. Kiisk, A. Krasnikov, M. Nikl, I. Sildos, Y. Usuki, and S. Zazubovich, *Red emission of $PbWO_4$ crystals*, Radiation Measurements **38**, 623–626 (2004).

X K. Saal, M. Plaado, I. Kink, A. Kurg, V. Kiisk, J. Koževnikova, U. Mäeorg, A. Rinken, I. Sildos, T. Tätte, and A. Lõhmus, *Aminopropyl embedded silica films as potent substrates in DNA microarray applications*, Mater. Res. Soc. Symp. Proc. **873E**, K9.3 (2005).

XI P. Fabeni, V. Kiisk, A. Krasnikov, M. Nikl, G. P. Pazzi, I. Sildos, and S. Zazubovich, *Tunneling recombination processes in $PbWO_4$ crystals*, phys. stat. sol. (c) (2006), submitted.

1. INTRODUCTION

1.1. Technological interest in luminescent materials

There is a continuous technological interest in the design of efficient and durable luminescent materials. The range of applications is extremely broad: such materials are required in various lightning and display devices (fluorescent lamps, cathode-ray tubes, plasma display cells), photonic devices (light emitters, amplifiers, lasers), detectors (X-ray screens, scintillators) [1, 2]. Prospective applications also include fluorescence-based chemical sensors [3, 4]. Most luminescent materials presently in use are based on the emission of some intentionally incorporated impurities. Impurity activation of transparent crystalline or glassy materials is a powerful method for designing phosphors for specific needs. Transition metals and rare earths are two broad classes of impurities that have found widespread use. In this thesis we confine our attention to rare earths. Rare-earth-based luminescent materials are being continually developed for a range of applications including lasers [5], displays [2, 6, 7], scintillators [8], *etc.* As specific examples of widely used rare earth phosphors, one could mention Y_2O_2S:Eu^{3+} that is the common red phosphor in cathode ray tubes, Gd_2O_2S:Tb^{3+} is used in X-ray intensifying screens, Y_2O_3:Eu^{3+} is responsible for the red emission component in fluorescent lamps and plasma display panels, Er^{3+}-doped silica fibre amplifiers are used in optical communication, Nd^{3+}:YAG has become a very popular laser host [1]. The two basic requirements for any phosphor material are the high luminescence yield and long-term stability. In optical and optoelectronic applications the possibility to prepare the materials in a waveguide geometry is required. On the other hand, low-temperature optical gas sensing applications might prefer the materials in the form of nanoporous powders since the sensing mechanism usually involves some surface reaction. In relation to gas sensing, further consideration about the sensitivity and selectivity of the fluorescence on the different chemical species is required.

From the point of view of luminescence applications in visible and UV spectral ranges, wide band gap materials are attractive hosts for optical activation with impurities (like rare earths). In these materials the impurity can emit within the optical window of the host material. In addition, the emission of rare earth impurities in insulators does not suffer from the temperature quenching effects that are inherent to semiconductor hosts (as *e.g.* Auger energy transfer to free carriers). Wide-gap materials are also attractive for application under UV, VUV, or X-ray excitation. For example, such materials are essential for various UV and VUV downconversion phosphors, based on either quantum cutting mechanism [9] or multiplication of electronic excitations [10]. Within the wide-gap materials our major attention has been focused on various metal-oxides since oxides are generally less sensitive to oxygen surface contamination and also the preparation route of the materials is relatively simple.

1.2. Group IVa dioxides as wide band gap optical materials

1.2.1. TiO_2 (titania)

There exists three crystalline modifications of TiO_2 in nature: rutile, anatase, and brookite. Anatase is a stable phase at room temperature, at higher temperatures it transforms to rutile; brookite occurs only when stabilized by some impurities. Most natural as well as artificial single crystal formation processes lead to the rutile phase, which is therefore the most common form of TiO_2. In the present work we are interested only in the rutile and anatase phases, which have also been most intensively studied by different research groups. Rutile is a denser phase and, correspondingly, exhibits higher refractive index (table 1). Both modifications have a tetragonal unit cell. It is convenient to consider the crystal structures of all polymorphs of TiO_2 as networks of differently coordinated TiO_6 octahedra [11]. Such octahedron is also the common building block in various titanates (like $SrTiO_3$ and $BaTiO_3$), which allows a comparison of the optical processes and impurity centers in these matrices.

Most traditional applications of TiO_2 (as *e.g.* white pigment) do not depend on the crystalline modification used and the rutile as the most abundant phase is mainly applied. During the last 10–15 years, however, some striking differences between the electronic, optical, and photocatalytic properties of rutile and anatase have been noticed.

TiO_2 offers two unique properties under UV-irradiation: a distinguished photocatalytic activity (strong oxidation power) [12, 13] and super-hydrophilicity [14]. These properties have found application in self-cleaning and antifogging coatings, degradation of toxic compounds in environment, and photolysis of water for producing hydrogen. The particular photocatalytic activity of anatase has been applied in an electrochemical photovoltaic cell of a promising efficiency [15].

The basic optical properties of TiO_2 have been widely studied. It is known that a band-to-band excitation of TiO_2 leads to the formation of free exciton states in TiO_2 of rutile phase [31] and, due to a strong exciton-phonon coupling, self-trapped exciton (STE) states in TiO_2 of anatase phase [32–34]. The recombination of STE at low temperatures results in a broad ($\sim$0.5 eV) gaussian-shaped emission spectrum with the intensity maximum at approximately 2.3 eV. The STE emission is almost fully quenched at room temperature.

Interestingly enough, it has been noticed that the decay of the STE emission follows a single exponential function only when excited near the onset of the fundamental absorption [35, 36]. This corresponds to the immediate formation of the STE state through the localization of the photoexcited electron-hole pair within a TiO_6 octahedron. The decay time of the STE state at 5 K is about 1.5 μs. For excitation energies well above the band gap energy, a power-law component $I(t) \propto (1 + t/\tau)^{-m}$ with $m \sim 1$ dominates in the decay kinetics indicating that spatial separation of the photoexcited electron-hole pair takes place. As $m \neq 2$, the power law decay cannot be attributed to a simple bimolecular recombination between freely migrating charge carriers. Instead, the behavior is characteristic of a tunnelling recombination between randomly distributed localized electrons and holes [37, 38].

Table 1: Some basic properties of TiO_2, ZrO_2, and HfO_2 at ambient conditions.

	TiO_2		ZrO_2, HfO_2		
	Rutile	Anatase	Monocl.	Tetrag.	Cubic
Density (g/cm^3)	4.25[a]	3.89[a]	5.81[f]	6.08[f]	6.22[f]
			10.11[f]	9.96[f]	10.67[f]
Refractive index	2.70[b]	2.56[c]	2.21[g]	2.19[h]	2.12[i]
			2.16	–	–
Optical bandgap (eV)	3.0[d]	3.2[d]	4.70[j]	5.22[k]	–
			5.68[l]	–	–
Static dielectric constant	114[e]	31[e]	20[m]	47[m]	37[m]
			16[m]	70[m]	29[m]

[a] Ref. [16]
[b] Ref. [17] (at 600 nm)
[c] Ref. [18] (at 550 nm)
[d] Ref. [19]
[e] Ref. [20]
[f] Refs. [21–23] (theoretical values according to structural data)
[g] Ref. [24]
[h] Ref. [25] (at 632.8 nm)
[i] Ref. [26] (at 632.8 nm)
[j] Ref. [27]
[k] Ref. [28]
[l] Ref. [29]
[m] Ref. [30] (theoretical estimates)

The detailed model and the formation process of STE is not established up to now. Yet, polarized photoluminescence study have offered some insight into the problem. Our previous study of single-crystal anatase has shown that the STE emission is strongly polarized with the electric vector predominantly perpendicular to the optic axis of the crystal [39]. The observation has led to the hypothesis that the recombination of STE state involves mainly the relaxation of neighboring oxygen atoms in the plane perpendicular to the axis of the octahedron. In that case the formation of STE in TiO_2 might be quite similar to the corresponding process in alkali- and alkali-earth halides where the so-called V_K center is formed through the autolocalization of a hole between two neighboring oxygen atoms [40]. The polarization properties of STE emission have proved to be useful for examination of crystallite orientation in anatase films [41].

1.2.2. ZrO_2 (zirconia) and HfO_2 (hafnia)

ZrO_2 and HfO_2 could be called twin oxides as they exhibit remarkably similar physical and chemical properties (see Table 1). Both oxides exist in three polymorphs under ambient pressure. At low temperatures the only thermodynamically stable phase is the monoclinic one; at higher temperatures it transforms first to a tetragonal phase and then to a cubic structure. The transition temperatures are 1170 K and 2370 K for ZrO_2 [42] and 1730 K and 2600 K for HfO_2 [43]. Both monoclinic and tetragonal phases can be considered as distorted cubic structures [44]. The monoclinic phase is less symmetric than the tetragonal one. The tetragonal and cubic polymorphs, being frequently found technologically more attractive, can

be stabilized at room temperature either by adding small amounts of divalent or trivalent impurities (like yttrium or calcium) or by preparing the material in a nanostructured form (*e.g.*, as nanosized films and powders) [28, 45]. Monoclinic ZrO_2 (containing a small amount of hafnium) is found in nature in small quantities as the mineral baddeleyite.

The extraordinary similarity of zirconia and hafnia is attributed (besides the homological outer shell configurations $[Kr]4d^25s^2$ and $[Xe]4f^{14}4d^25s^2$ of Zr and Hf) mainly to the lanthanide contraction of Hf that is responsible for the similar atomic and ionic radii of Zr and Hf atoms as well as their similar ionization potentials [46]. Yet, some minor differences exist. For example, HfO_2 is more stable in contact with Si (important for microelectronics technology) whereas ZrO_2 is of superior hardness.

The optical properties of ZrO_2 and HfO_2 have not been so thoroughly studied as those of TiO_2. Some experimental evidence about intrinsic emission has been reported. Under a band-to-band optical excitation high-quality monoclinic HfO_2 materials exhibit broad Gaussian-shaped emission band centered at 4.3–4.4 eV [47, 48]. A similar emission band of monoclinic ZrO_2 is located at 4.2–4.3 eV [48]. There are several indications of a self-trapped excitonic origin of this emission: it is always present in high-quality pure crystalline matrices, its excitation onset coincides with the onset of the fundamental absorption of the material with the spectral shape being independent on the excitation energy, it exhibits large Stokes' shift, its decay time is in the μs range (at low temperatures), and it quenches at higher temperatures (in hafnia it is still present at room temperature). Furthermore, narrow features in the excitation spectrum near the fundamental absorption edge has been attributed to free exciton absorption. As in the case of TiO_2, these optical manifestations of excitonic states are quite sensitive to the purity and crystalline form of the matrices and can be used to characterize the material's structure and quality. For example, in defective ZrO_2 matrices the intensity of the STE band is markedly reduced and several emission bands at lower energies appear under a band-to-band excitation. These latter emissions can be excited also within the forbidden gap of zirconia indicating their defect-related origin.

Besides the monoclinic form of zirconia there are also several reports on the luminescence of the yttria-stabilized cubic form, which is generally of greater technological importance (see [49] and the references therein). These luminescence bands characterize mainly various intrinsic and extrinsic F-centers.

In all three oxides (TiO_2, ZrO_2, HfO_2) the band-to-band excitation of an electron corresponds to a charge transfer process because the top of the valence band is composed primarily of O^{2-} $2p$ states whereas the bottom of the conduction band arises mainly of the Ti^{4+} $3d$ [50], Zr^{4+} $4d$ [51], or Hf^{4+} $5d$ [43] orbitals, respectively.

One of the most promising application of hafnia and zirconia have been in optical coatings [52–54]. Besides their high refractive index, UV-visible transparency and mechanical strength, a particular property of interest for application in optical coatings is their high optical damage thresholds [53, 54], which is essential in *e.g.* laser-ignited thermonuclear fusion systems. Recently, however, the main interest in these oxides (and particularly in hafnia) is related to the microelectronics in-

dustry. It is well-known that the current technology of microelectronics devices is based on silicon and silica (SiO_2). The silica has the special role as a gate dielectric in metal-oxide-semiconductor (MOS) field-effect-transistors and capacitor structures. The combination of silicon and silica has been very successful due to the high-quality stable interface between the materials and the success in preparing uniform thin amorphous layers of these materials. The continuous downscaling of microelectronic circuits is approaching the limit where the leaky currents through the silica layers of a few nanometers in thickness are leading to significant power dissipation. For that reason an active research on alternate gate dielectrics has been taking place during the last few years. A series of promising candidates has been found [55]. It has been now generally agreed that hafnia or hafnia-silica mixed oxide is the most probable replacement for silica in the near future. A further investigation of the peculiarities of the materials as well as improvement of the preparation methods are needed.

1.3. Rare earth ions as optical dopants

1.3.1. Introduction

There exists two classes of chemical elements with partially filled inner electronic shells: transition metals and rare earth metals. There are two series of rare earths: lanthanides and actinides. We are interested only in the lanthanides, which comprise the group of 14 transition elements starting with lanthanum (La) and ending with ytterbium (Yb). Hereafter we mean by rare earths (REs) the lanthanides.[1] The position of REs as well as the order of orbital filling can be most clearly shown in the extended view of the periodic table of elements (Fig. 1.1). It is energetically favorable that the $4f$ orbitals become populated only after the $5s$, $5p$, and $6s$ shells are occupied. The electronic configuration of REs can thus be described by $[\mathrm{Xe}]4f^n6s^2$, with n ranging from 1 to 14.[2]

H																									He	1*s*
Li	Be																	B	C	N	O	F	Ne	2*s* 2*p*
Na	Mg																	Al	Si	P	S	Cl	Ar	3*s* 3*p*
K	Ca											Sc	Ti	V	Cr	Mn	Fe	Co	Ni	Cu	Zn	Ga	Ge	As	Se	Br	Kr	4*s* 3*d* 4*p*
Rb	Sr											Y	Zr	Nb	Mo	Tc	Ru	Rh	Pd	Ag	Cd	In	Sn	Sb	Te	I	Xe	5*s* 4*d* 5*p*
Cs	Ba	La	Ce	Pr	Nd	Pm	Sm	Eu	Gd	Tb	Dy	Ho	Er	Tm	Yb	Lu	Hf	Ta	W	Re	Os	Ir	Pt	Au	Hg	Tl	Pb	Bi	Po	At	Rn	6*s* 4*f* 5*d* 6*p*
Fr	Ra	Ac	Th	Pa	U	Np	Pu	Am	Cm	Bk	Cf	Es	Fm	Md	No	Lr	Rf	Db	Sg	Bh	Hs	Mt	Ds	Rg							7*s* 5*f* 6*d* 7*p*

Figure 1.1: The extended view of the periodic table of elements. Accentuated cells contain the rare earths. The order of orbital filling along a series is shown.

The distinct optical and magnetic nature of REs arises from the partially filled

[1] The term "rare earth" is of historical origin and is actually not very appropriate as the lanthanides are neither rare in abundance nor are they "earths", which is an obsolete term for oxides. However, due to its widespread usage we accept this term in this writing.

[2] There are some exceptions. Lanthanum and gadolinium have configurations $[\mathrm{Xe}]5d^16s^2$ and $[\mathrm{Xe}]4f^75d^16s^2$, respectively, because half- and fully-filled subshells exhibit unusual stability.

$4f$ subshell which is effectively shielded from the external influences by the filled $5s^2 5p^6$ shells. This is in contrast to the partially filled d orbitals of the transition metals which are strongly affected by the surrounding environment. The screening of $4f$ electrons becomes more effective as the atomic number increases. Starting from Nd the $4f$ wavefunction already has its maximum inside the $5s^2 5p^6$ shells [56]. It is evident that the $4f$ electrons cannot participate significantly in chemical bonding. Due to the identical configuration of the shells, the RE elements behave chemically quite similarly, so that before the invention of modern chemical techniques these elements were considered rare and difficult to separate.

REs are strongly paramagnetic, hence the salts of REs have been quite extensively applied in superconductors, magnetic refrigeration, permanent magnets, *etc.* The partially filled $4f$-shell also gives rise to unique optical properties which provide the basis for the optical applications of REs. Most importantly, the $4f$ electrons remain highly localized to the atom and the optical transitions within the $4f$ manifold maintain much of an atomic-like character even when the RE ion is embedded into a solid.

1.3.2. Energy level structure

It is well-known that free atoms or ions generally exhibit discrete energy level scheme. However, of primary technological interest are not the optical properties of the free RE atoms but rather those of the RE ions embedded into a solid. It has been found that when introduced into a solid the electronic configuration of RE ion usually acquires the trivalent charge state $[\mathrm{Xe}]4f^{n-1}$ (*i.e.*, the two $6s^2$ electrons and one $4f$ electron is removed). This is due to the fact that it takes relatively little energy to remove one electron from the $4f$ shell (the two $6s$ electrons are loosely bound anyway). For energies from IR up to the UV range, the transitions in trivalent RE ions only involve the energy levels of the $4f$ shell, *i.e.* the ground configuration of the ion [57]. As the $4f$ shell of RE ion is still shielded by the $5s^2 5p^6$ electrons, the free-ion energy levels are only weakly perturbed by the surrounding environment and the $4f$ intraconfigurational transitions retain their atomic-like characteristics, *e.g.* spectral sharpness (of the order of $10\,\mathrm{cm}^{-1}$ in good crystalline host) and long lifetime (of the order of 1 ms). From the scientific as well as the technological point of view one is mostly interested in the spectrally narrow highly efficient emission of the RE ions. At liquid helium temperatures, where the optical dephasing processes are negligible, the homogeneous spectral linewidth of individual emitters approaches the radiative lifetime-limited value. For example, it has been demonstrated that the linewidth of the $4f$ transitions of Eu^{3+} ion in Y_2SiO_5 (radiative lifetime 2.6 ms) can be as narrow as 122 Hz [58], which is the narrowest optical resonance found in a solid. Such narrow lines provide sensitive probes of weak perturbations. For example, the Stark splitting of the emission lines in a crystal field and the relative intensity of different transitions are indicators of the site symmetry of the emission center. Technologically the phosphors emitting spectrally narrow lines are favorable in *e.g.* display devices, where they can provide very pure primary colors (the red emission of Eu^{3+} at 620 nm being the most well known).

Actually, the sharpness of electronic transitions is not the unique property of rare earths as several transition-metal-activated systems expose line spectra as well. Rather, the most intriguing property of trivalent rare earth ions is that the spectral position of the emission lines is almost independent of the host lattice. For example, possibly the most intense research is oriented to optoelectronic materials containing Er^{3+} ions having an emission band around 1535 nm which happens to coincide with the principal low-loss window in the absorption spectrum of aluminosilicate optical fibre [59]. Due to the insignificant dependence of the RE emission wavelength on the host material one can compile quite universal energy level scheme for the description of the essential absorption and emission bands of such ions, the so called "Dieke diagram" [57]. The crystal field effects can be treated as a perturbation that merely induces shifts and splittings of the free-ion energy levels. The optical transitions within $4f$-shell exhibit also very weak electron-lattice coupling, therefore very intense sharp zero-phonon lines are observed and the phonon sideband is practically absent (*i.e.* Debye-Waller factors are close to unity).

For later reference, let us summarize the notation of atomic energy levels. In the treatment of multielectron atoms one usually starts from the central-field approximation, where each electron is considered moving independently in an effective self-consistent central (spherically averaged) field due to the nucleus and all other electrons. This approach enables describing each quantum state of the N-electron atom by an electronic configuration $(nl)_1(nl)_2 \dots (nl)_N$, where n is the principal quantum number (electronic shell) and l is the orbital quantum number (subshell). The orbital quantum number ranges from 0 to $n-1$ and is denoted (for historical reasons) by letters $s, p, d, f, \dots$ (in order of increase). Subshell with orbital quantum number l contains $2l+1$ orbitals, each of which can accommodate up to two electrons with opposite spins. Therefore $4f$ subshell can hold up to 14 electrons. Subsequently to the central field approximation all weaker interactions (as non-central electrostatic and spin-orbit interactions) are treated as perturbations. In order to classify the quantum states of an electronic configuration according to the remaining interactions there exists two main approaches. In the Russell-Saunders or LS-coupling scheme it is assumed that the spin-orbit interactions are much weaker than the spin-spin and orbit-orbit interactions between individual electrons, so that the quantum state is described by the total spin moment $\boldsymbol{S}$ (quantum number S) and the total orbital angular moment $\boldsymbol{L}$ (quantum number L). Finally, $\boldsymbol{S}$ and $\boldsymbol{L}$ couple to form the total angular moment $\boldsymbol{J}$ (quantum number J). It is customary to denote the quantum state in LS-coupling by ${}^{2S+1}L_J$. The projection J_z of $\boldsymbol{J}$ along an z axis can acquire values within $-J \dots J$, so that the state ${}^{2S+1}L_J$ is $2J+1$ times degenerate. In a crystalline environment the degeneracy is at least partly lifted (depending on the symmetry of the site). According to the theorem of Kramers, if the ion possesses an odd number of electrons, the Stark components of ground state remain at least two-fold degenerate in any crystal field. In the other extreme, where the spin-orbit coupling of individual electrons are considered as the strongest, one employs the j-j coupling scheme. It has been found that the LS-coupling describes the lighter elements, where the electrostatic interaction is relatively strong, whereas in the heavier atoms the j-j coupling is

more appropriate. The RE atoms lie somewhere between and neither coupling scheme is wholly appropriate. More accurately, the quantum states of RE atoms and ions can be described as an intermediate coupling states, which can be considered as mixed states (linear combinations) of several LS states [60]. Nevertheless, for classification of the electronic states, one usually utilizes the LS notation. In this case $^{2S+1}L_J$ denotes the prevalent contribution to the given quantum state. The LS notation is most appropriate for the states near to the ground state. The effect of mixing is relatively small on the energy of the levels but can be significant on the optical transition probabilities between the states.

The ground state in the LS-coupling can be derived from the Hund's rules. These rules say that in the ground state electrons are distributed in a manner that maximizes S, and within the terms exposing the same S, the one with the highest value of L lies energetically lowest. Finally, within the levels with the same S and L, the one with the smallest J lies lowest (applicable if the shell is less than half-filled). For example, the ground levels of Sm^{3+} and Eu^{3+} are $^6H_{5/2}$ and $^7F_0$, respectively.

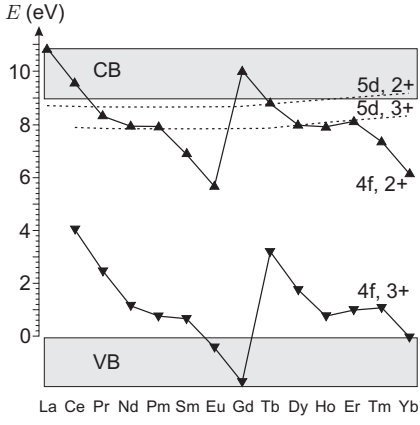

Figure 1.2: Relative positioning of RE^{2+} and RE^{3+} ground state energy levels in $4f^N$ and $4f^{N-1}5d$ configurations with respect to the host energy bands in YPO_4 [61].

Since all states inside a configuration possess the same parity in inversion-symmetric environment, electric dipole transitions between such states are forbidden. Such situation is always realized for free ions. Nevertheless, the transitions observed in triply ionized RE ions in crystals are mainly of electric dipole nature with typical oscillator strengths around 10^{-6} and corresponding lifetimes around 1 ms. This is attributed to the partial mixing of different parity states by the crystalline environment. Such transitions are called forced electric dipole transitions. In addition to these transitions magnetic dipole and electric quadrupole transitions are also sometimes observed.

In ionic matrices divalent and tetravalent charge state is also sometimes encountered mostly due to the extraordinary stability of half- and fully-filled shells. Such special cases are Ce^{4+} ($4f^0$), Eu^{2+}, Tb^{4+} ($4f^7$) and Yb^{2+} ($4f^{14}$). This is also evident from the systematic behavior of the ground state energies of di- and trivalent ions (Fig. 1.2). In these ions the interconfigurational optical transitions between the $4f^N$ ground configuration and the $4f^{N-1}5d$ excited configuration are important. Trivalent RE ions also exhibit $5d-4f$ transitions, but usually in VUV range (an exception being Ce^{3+}). These transitions involve energy levels of different parity and are therefore electric dipole allowed. There is generally a strong coupling of $5d$ states with crystal lattice (phonons), therefore the energies of these states are significantly influenced by the

environment and frequently broad vibronic emission and excitation bands arise due to the transitions involving these states. However, as the RE ions (of the same charge state) expose similar valence states and similar ionic radii, it is of no surprise that the energies of $5d$ states are nearly the same (within $\sim$0.5 eV) for each RE ion when in the same site in the same compound [61] (Fig. 1.2).

In addition to the excitation within the $4f^N$ or $4f^{N-1}5d$ configuration there exists another possibility of direct excitation of RE^{3+} ions. This involves transfer of an electron from the valence band of the host matrix (*i.e.* from a neighboring anion) to the $4f$ level of the corresponding RE^{2+} ion. Such transition gives rise to the charge transfer (CT) absorption band. The hole left behind in the valence band is attracted by the divalent ion and the system is described as a CT state (CTS). An intersystem crossing of CTS to an excited $4f$ state of RE^{3+} ion can take place leading to a luminescence within the $4f$ manifold. Eu^{3+} is known to exhibit a strong CT absorption. For example, efficient CT absorption of UV radiation in Y_2O_3:Eu^{3+} (the red phosphor used in fluorescent tubes) takes place leading eventually to the luminescence from the ^5D_J levels of Eu^{3+} [1]. The CT absorption band is relatively broad ($\lesssim$1 eV) due to a lattice relaxation. It has been argued that the CT transition essentially starts from the top of the valence band and hence the CT energy represents closely (within 0.5 eV) the energy of the RE^{2+} ground state with respect to the top of the valence band [61]. These findings provide a method for estimating the energy levels of the RE ions with respect to the band edges of the host material [61, 62]. Knowledge of these relative energy levels helps understanding various host-guest interactions as *e.g.* charge carrier trapping by the impurity and impurity autoionization.

1.3.3. Efficiency of luminescence

The overall efficiency of an impurity-activated phosphor can be viewed as a product of two factors: the efficiency of excitation and that of emission. First, let us consider the latter, that is influenced by the presence of nonradiative relaxation channels. One of the most important nonradiative process is the relaxation into energetically close levels via multiphonon emission. Such process can be dominant if the energy levels of the impurity atom are closely spaced. Namely, the rate of phonon emission connecting energy levels ΔE apart, is proportional to $\exp(-k\Delta E/\hbar\omega_{\max})$, where $\hbar\omega_{\max}$ is the maximum energy of phonon coupled to the emitting states [60]. The presence of large gaps ΔE between the initial and the final electronic level of RE ion reduces the probability of nonradiative decay. For example, this accounts for the high yield of luminescence from the levels $^5D_0$ of Eu^{3+} and $^5D_4$ of Tb^{3+}. As for the host lattice, the highest phonon frequencies are responsible for the nonradiative relaxation. The lower the energy of the host phonons the larger is the number of phonons connecting the emitting level with the terminal level reducing the probability of nonradiative transition. As a simple rule, if more than ten phonon are required to connect the emitting level to the next lower level, the multiphonon emission can be considered negligible. Conversely, the luminescence will be totally quenched if fewer than four phonons are required [63]. An outline of the phonon density of states of a crystalline matrix can be obtained

from Raman scattering and IR absorption spectra. The highest phonon frequencies of TiO_2 (anatase), ZrO_2 (m), and HfO_2 (m) lattices remain below $640\,cm^{-1}$ [64], $650\,cm^{-1}$ [65], and $680\,cm^{-1}$ [65, 66], respectively. These values are quite low in comparison to other widely used hosts (for example, the stretching frequencies of Al_2O_3 and SiO_2 are $870\,cm^{-1}$ and $1100\,cm^{-1}$, respectively). Therefore, one could expect these metal-oxides to be suitable hosts for RE activation.

The second important mechanism influencing luminescence yield is ion-ion interaction that becomes noticeable at relatively high impurity concentrations (or clustering of impurities in the case of low solubility in the host). During such an interaction an energetic relaxation within one ion leads to a resonant excitation of its neighboring ion. The atom releasing energy is called donor and the one gaining energy is called acceptor. This energy transfer leads to one of the three types of effects: a co-operative upconversion, an energy migration, or cross-relaxation [59]. In the first case, occurring at high pumping rates, ions in the metastable state decaying to the ground state can couple in such a way that the decay of an ion promotes nearby ion into a higher level. Energy migration, as the name implies, is the resonant energy transfer between the same pair of levels of the same type of ions. The essential loss mechanism is the cross-relaxation, whereby excitation energy from an ion decaying from a highly excited state promotes a nearby ion from the ground state to an excited level. Cross-relaxation is thus the reverse of upconversion. Upconversion and cross-relaxation take place if there is an accidental match of different transition energies.

Finally, there can exist nonradiative relaxation paths related to Auger-type energy transfer to either free carriers or nearby defect states. The first situation can be considered insignificant in large gap ionic crystals where the charge carrier concentration is negligible but can be substantial in doped semiconductors (*e.g.*, in the technologically important system Er^{3+}:Si).

A manifestation of the ion-ion interactions is the non-exponential decay of luminescence. This follows from the statistical distribution of the donors and acceptors and the fact that the energy transfer probability depends on the distance between donor and acceptor. Assuming that only one kind of energy transfer from acceptors to donors takes place, the following expression for the decay kinetics is obtained [67]:

$$I(t) = I_0 \exp\left\{-\frac{t}{\tau_0} - \Gamma\left(1-\frac{3}{s}\right)\frac{n}{n_c}\left(\frac{t}{\tau_0}\right)^{3/s}\right\}, \tag{1.1}$$

where τ_0 is radiative lifetime, n is the acceptor concentration, n_c is a critical acceptor concentration, and $s = 6, 8, 10$ for dipole-dipole, dipole-quadrupole, and quadrupole-quadrupole interaction, respectively.

In strongly disordered systems a stretched-exponential decay is frequently encountered:

$$I(t) = I_0 e^{-(t/\tau_0)^{\beta}}.$$

τ_0 and β are fitting parameters. The decay can be connected to a distribution of decay rates with the average lifetime $\langle\tau\rangle = \tau_0\Gamma(1+\beta^{-1})$ [68]. Such non-exponential

decay can arise of the presence of a range of different sites for the emitting center or a distribution of de-excitation channels.

1.3.4. Excitation mechanisms

Another important aspect of a luminescent material is the efficiency of impurity excitation. As the concentration of the emitting impurities is usually kept relatively low in comparison to the amount of the host material, one is primarily interested in the possibility of an indirect excitation of the impurities through the host excitation. This is especially true for trivalent RE impurities whose $4f$ transitions expose very small direct absorption cross sections (10^{-21}–$10^{-20}\,\mathrm{cm}^2$) owing to the long lifetime of the excited state. In the case of an indirect excitation the optical dopant behaves basically as an efficient radiative recombination center for the electrons and holes of the host material.

Electrons can be efficiently excited from the host valence band to the conduction band by various processes like the absorption of visible or UV radiation within the fundamental absorption band, bombardment with electrons (as in CRTs), or electrical injection of charge carriers (as in LEDs). The free charge carriers can combine to form neutral electronic excitations like free and trapped excitons. The question arises how can these electronic excitations of the host matrix mediate the excitation energy to the emission center. The free carriers and free excitons are very mobile, but recombine in the time scale of $10^{-9}\,\mathrm{s}$. The self-trapped excitons migrate much more slowly through the hopping diffusion. However, at low temperatures the STEs can survive for about $10^{-6}\,\mathrm{s}$ and at higher temperatures their hopping probability is increased, so that the average migration range of STEs is almost the same as that of free excitons: typically of the order of 10 nm, corresponding to the average distance between two RE centers for an homogeneous doping level of 0.1%. After migration to the RE impurity one of the following mechanisms is usually involved in the energy transfer process [69].

(i) Radiative energy transfer

(ii) Resonant non-radiative energy transfer from an exciton bound to some (possibly impurity-related) defect or an intentionally incorporated sensitizer. The process takes place through dipole-dipole or some higher-order interaction as mentioned previously. The probability of the process is essentially determined by the distance between the energy donor and acceptor (depending on the type of interaction) and the overlap integral of the corresponding emission and absorption spectra [70].

(iii) Impact excitation by hot electrons. This process can be effective only at high electric field in high-quality crystals with large mean free path of mobile carriers (*e.g.* electroluminescence from reversely biased p-n junction [71]). In the case of photoexcitation the fast energy relaxation with a characteristic lifetime of $10^{-12}\,\mathrm{s}$ renders this process unlikely.

(iv) An Auger-type process where the relaxation of impurity-bound exciton induces excitation of the impurity center through a Coulomb interaction. An additional free or bound electron can favor the energy conservation in the

Auger process. The process is believed to be essential in a number of RE-doped semiconductor systems like InP:Yb^{3+} [72], SiO_2:Er^{3+} [73], Si:Er^{3+} [59].

Note that due to the energy transfer from host to guest the impurity emission can be considered as a probe for studying the migration of electronic excitations.

1.4. Aim of the present work

This PhD work is mostly an experimental investigation of fundamental optical processes in pure and RE-doped TiO_2, ZrO_2, and HfO_2 with a main intent of developing novel RE-activated phosphors. Possibilities of novel applications of the materials (as waveguides, chemical sensors, and scintillators) will be evaluated. The work is partly a continuation of the master's thesis of the author and partly suggested by the unique combination of materials, dopants, and preparation methods available for study. Europium was chosen as a dopant because it is one of the most important emitter in the visible range. In addition, the spectroscopic properties of Eu^{3+} make it attractive as an optical probe of the crystalline environment. Samarium is another impurity exposing strong visible emission. The similar size of Eu and Sm ions make a comparative study possible. Sm^{3+} has not been studied in HfO_2. Here a systematic optical study of the ions in metal-oxides will be presented. Luminescence methods will be mainly applied as the impurity absorption cannot be observed in the films of $\sim$100 nm in thickness.

The material presented in this thesis is organized as follows. The present chapter intended to cover the background. Chapter 2 introduces the reader to the principles of the thin film preparation methods applied in the work including atomic layer deposition, sol-gel technique, and ion implantation. The original investigation comprises the final two chapters. Chapter 3 describes the study of the waveguiding properties of atomic layer deposited films (pure and Sm-doped TiO_2) and chapter 4 describes the results of developing rare-earth-doped metal-oxide luminescent materials.

2. PREPARATION OF PURE AND DOPED METAL-OXIDE MATERIALS

2.1. Introduction

A wide range of methods for preparing both pure as well as doped thin films and powders of TiO_2, HfO_2 and ZrO_2 has been developed including chemical vapor deposition [29, 74], sol-gel technique [11, 45, 75–82], various sputtering techniques [11, 27, 28, 33, 83, 84], electron-beam evaporation [53], liquid phase deposition [85], spray pyrolysis [86, 87], pulsed laser deposition [52], and several others. The choice of preparation method depends on several factors including the intended application of obtained materials and the production cost. In electronic, optical, and optoelectronic devices the films should usually be dense, homogeneous and exhibit smooth surfaces. On the other hand, for catalysts and gas sensing the films with rough surfaces, nanostructure, and/or significant porosity are sometimes preferred. There are also applications (scintillators, phosphors) that does not put forward any specific demands other than acceptable luminescence yield and long-term durability. In the present work we employed two methods for preparing optical and luminescent materials: atomic layer deposition and sol-gel method. The development of the former technique has relatively long traditions in our Institute and thin films of quite well-predicted properties can be obtained. Sol-gel technique was developed as an inexpensive alternative enabling *in situ* doping of materials.

2.2. Atomic layer deposition

Atomic layer deposition (ALD) is a variant of chemical vapor deposition (CVD). In contrast to CVD, which relies on the continuous reaction between simultaneously introduced precursor gases, the ALD process is based on sequential application of two complementary surface reactions [88]. Hence the precursor gases are alternatively introduced into the reaction chamber. The precursor materials are chosen so as to ensure self-limited deposition during every reaction step. The precursor pulses are separated by purge cycles to remove reaction by-products and the precursor molecules that have not been involved. The first precursor is chemisorbed until the surface is saturated. The second precursor reacts with the chemisorbed species (this is usually an exchange reaction). When the reaction completes, the film growth cannot proceed further until the previous precursor is introduced again. Ideally, each growth cycle would result in a monolayer of thickness increase. In reality, however, tens of cycles are required. The reduced growth rate is more probable in the case of large precursor molecules which can temporarily block several adsorption sites. Yet, the final thickness of the film can be quite accurately predicted based on the number of growth cycles used (contrary to the conventional CVD process, where the deposition time determines the film thickness). Furthermore, various methods, like quartz crystal microbalance [89, 90] and incremental reflection [91, 92], can be applied for *in situ* monitoring of the film growth. Due to the self-limiting nature of the surface reactions, the ALD can be used for covering

large and complex-shaped (*e.g.* profiled) areas with uniform film.

Suitably chosen substrate material and growth conditions can lead to an epitaxial[3] growth of the film. In such case one talks about atomic layer epitaxy (ALE). Generally, however, the oriented growth of crystalline phase takes place on several nanosized areas independently so that polycrystalline structure develops and the surface roughness increases with the film thickness. At lower substrate temperatures the growth might be entirely disarranged so that amorphous films result. The amorphous structure usually also develops during the initial stage of the growth.

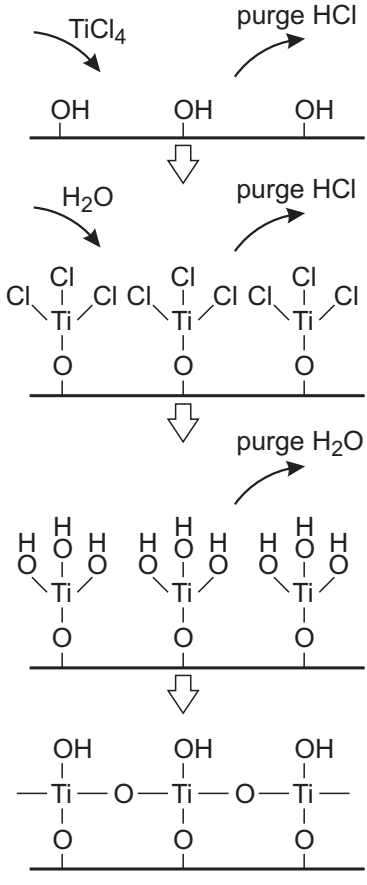

Figure 2.1: Steps of the chloride-based atomic layer deposition of TiO_2.

For atomic layer deposition of TiO_2, $TiCl_4$ [90, 93, 94], $Ti[(CH_3)_2CHO]_4$ (titanium isopropoxide) [95, 96] or TiI_4 [97] have been mainly used as titanium precursors whereby H_2O or O_2 have been used as oxygen source. Corresponding precursor materials are used for HfO_2 and ZrO_2 preparation as well (see [98–100] and the references therein). In the most common, chloride-based MeO_2 (Me=Ti, Zr, Hf) growth cycle the overall reaction taking place on the surface, is

$$MeCl_4 + 2\,H_2O \longrightarrow MeO_2 + 4\,HCl.$$

The steps of the process are illustrated in Fig. 2.1.

Up to now the atomic layer deposition of all the above-mentioned metal-oxides has been most intensively developed for application in microelectronics where conformal films need to be deposited at monoatomic layer precision. TiO_2, ZrO_2, and HfO_2 (or mixed oxides like $Hf_xSi_{1-x}O_2$) are presently seriously considered as alternative gate dielectrics in sub 65 nm CMOS technology due to the promising combination of high dielectric constant (80 for TiO_2 and 25 for HfO_2, ZrO_2), low leakage current, and good thermodynamic stability in contact with Si [55, 83]. Possibilities of employing for the purpose HfO_2-Al_2O_3 stacks (nanolaminates) grown via ALD have been recently demonstrated [101].

In addition, ALD films have been found to exhibit promising optical properties. ALD-grown thin films of TiO_2, ZrO_2, and HfO_2 are of uniform thickness and of reasonable optical losses in visible range showing clear interference fringes. This, in combination with the high strength and thermal stability of HfO_2 and

[3]Epitaxy is the regularly oriented growth of one crystalline substance upon another.

ZrO_2 and the hydrophilic [14] and self-cleaning [13, 84] ability of TiO_2 suggests application potential in optical coatings. Besides transmission, luminescence is another sensitive method for evaluating the optical quality of a material. For example, ALD-grown TiO_2 of anatase phase emits intrinsic photoluminescence that is very similar to the one found in high-quality single crystals [34]. Unfortunately, the *in situ* controllable doping of the films in the ALD process is sometimes a relatively complex task. For optical doping of ALD-grown film, one can use the ion implantation, for example.

2.3. Sol-gel technique

The sol-gel method is a wet chemistry process that is based on the gelation of a colloidal suspension (called "sol") and formation of a continuous inorganic network in liquid phase ("gel") [102]. The starting materials used in the preparation of the sol are usually inorganic metal salts or metal organic compounds such as metal alkoxides. Step-by-step the sol-gel process works as follows. First the metal alkoxide precursor is hydrolyzed through the addition of water to the solution. The hydrolysis reaction replaces alkoxide groups with hydroxyl groups producing alcohol:

$$-\overset{|}{\underset{|}{\mathrm{M}}}-\mathrm{O}-\mathrm{R} + \mathrm{H}-\mathrm{OH} \longrightarrow -\overset{|}{\underset{|}{\mathrm{M}}}-\mathrm{OH} + \mathrm{R}-\mathrm{OH}.$$

Here M denotes the metal atom. Subsequently several condensation reactions take place:

$$-\overset{|}{\underset{|}{\mathrm{M}}}-\mathrm{OH} + \mathrm{HO}-\overset{|}{\underset{|}{\mathrm{M}}}- \longrightarrow -\overset{|}{\underset{|}{\mathrm{M}}}-\mathrm{O}-\overset{|}{\underset{|}{\mathrm{M}}}- + \mathrm{H_2O}\,(\text{water condensation}),$$

$$-\overset{|}{\underset{|}{\mathrm{M}}}-\mathrm{O}-\mathrm{R} + \mathrm{HO}-\overset{|}{\underset{|}{\mathrm{M}}}- \longrightarrow -\overset{|}{\underset{|}{\mathrm{M}}}-\mathrm{O}-\overset{|}{\underset{|}{\mathrm{M}}}- + \mathrm{R}-\mathrm{OH}\,(\text{alcohol condensation}).$$

These reactions lead to the formation of colloidal particles of a diameter of a few hundred of nm consisting of polymerized metal-oxygen chains. During the gelation process these chains further join with each other (through the OH-groups) to form a conglomerate network of inorganic material. The sol solution can be used for preparing materials in various forms. By depositing the sol onto a substrate and drying at low temperature, one obtains porous material called xerogel. By high-temperature thermal treatment the xerogel further contracts and forms quite a dense material. Alternatively, one can precipitate the sol particles from the solution to form a nanopowder. It is also possible drawing fibers and SPM tips from the sol solution of suitable viscosity [103, 104]. If the liquid in a wet gel is removed under a supercritical condition, a highly porous and extremely low-density material called aerogel is obtained.

There are two basic sol-gel techniques for depositing thin films onto a substrate: dip-coating and spin-coating. In the dip-coating process the substrate is repeatedly dipped into the sol solution. The solution is attached to the surface due to cohesive, tenuous, and viscous forces. The main question arising is the dependence of the thickness h of a single coating on the withdrawal speed v and the properties of the

fluid (*i.e.*, viscosity η, density ρ, and surface tension σ). The question was long ago answered by Landau and Levich for dip-coating from an infinite bath in the limit when the surface forces dominate the viscous ones [105]:

$$h = 0.945 \frac{(v\eta)^{2/3}}{\sigma^{1/6}(g\rho)^{1/2}}.$$

This is the thickness of the wet layer of original solution immediately above the meniscus (Fig. 2.2). Subsequent evaporation, gelation, and densification (after annealing) of the film leads to a significant reduction of the thickness depending on the solid content in the original solution.

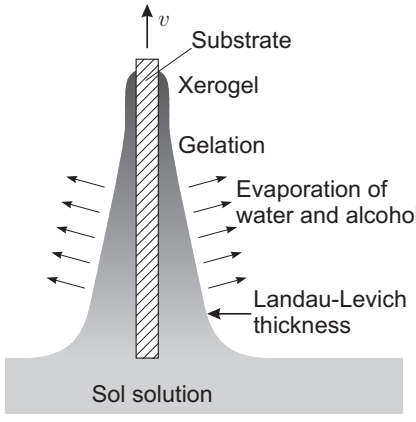

Figure 2.2: Sol-gel dip-coating process.

In the spin-coating process, the substrate spins at an angular speed ω around a vertical axis, that is perpendicular to the substrate surface, and droplets of solution are directed onto the surface along the rotation axis. Due to the centrifugal forces the solution flows radially outward and, to a quite good approximation, covers the substrate with an uniform layer.[4] As time goes on, the thickness of this layer decreases due to the continuous outflow and evaporation. Finally a thin solid layer remain, the thickness of which depends on various properties of the solution, as evaporation rate and solid content [106]. In practice one is frequently satisfied with a semi-empirical formula for the thickness,

$$h = A\omega^B,$$

where A and B are solution-dependent constants to be determined experimentally.

In comparison to other film deposition techniques the sol-gel process is considered quite inexpensive and simple (in the sense that it does not require complex apparatus). One can also point out excellent compositional control, homogeneity on the molecular level due to the mixing of liquid precursors, and low operation temperature. All these advantages doesn't mean, however, that films of desired properties are always readily obtained. Instead, long-standing experience is frequently needed to get the process under control. For example, careful choice of material composition and heat treatment as well as dust-free environment is needed to obtain waveguiding layers [75, 78]. The annealing at higher temperatures usually leads to crystallization of the film and considerable scattering losses at nanocrystallite interfaces. Likewise, the size and smoothness of the substrate and the convection in the ambient environment might strongly influence the uniformity of the deposited films. In luminescence applications (phosphors, scintillators)

[4] Rigorously speaking, if the liquid is Newtonian and if the initial thickness is uniform across the wafer, then the thickness profile at any following instance of time will also remain uniform.

the film is frequently not needed, rather the material can be prepared in the form of a nanopowder [80], thus eliminating the necessity for high-quality substrates.

2.4. Incorporation of impurities by ion implantation

Ion implantation is a low-temperature (as opposed to diffusion) technique for the introduction of impurities or defects into a solid matrix [107]. In the semiconductor technology it has almost entirely replaced the chemical (diffusion) doping. It has also found its place in other areas of scientific and technological activity. Ion implantation has several distinctive features as compared to diffusion and *in situ* methods: (1) large range of doses available; (2) extremely accurate dose control; (3) buried distribution (or layer) of impurities is possible; (4) low-temperature process; (5) chemical compatibility between the impurity and the host is not required; (6) less sensitive to surface cleaning.

During an ion implantation process the source material of impurity atoms is vaporized and ionized; after acceleration in electric field the ions of interest are selected by the charge-to-mass ratios and directed to the host target at well-defined energy and quantity. The most important parameters of ion implantation are therefore the final kinetic energy E_0 of the projectile particles and the total dose Φ (atoms/cm^2). The first one is set via the accelerating voltage whereas the second one is determined by the beam current, cross section, and time. By adjusting these two parameters one can quite accurately control the amount and distribution of the dopants. Ion energies usually range from 10^2 to 10^6 eV, resulting in dopant distributions with average depth from <10 nm to 10 μm. Doses range from 10^{11} atoms/cm^2 (trace concentrations) to 10^{18} atoms/cm^2 (buried layer).

As the accelerated ion enters into the target material, it undergoes a series of collisions with the host atoms until it finally stops at some depth. The *stopping power* is defined as the energy loss per unit path length of the ion: $S = -dE/dx$. For a given combination of the host and the implanted ion the stopping power is a function of ion energy E. It is usually possible to separate the stopping power into two parts.

$$S = -\left(\frac{dE}{dx}\right)_{\text{nuclear}} - \left(\frac{dE}{dx}\right)_{\text{electronic}}.$$

The first one is due to the collisions of the implanted ion with the host nuclei. The second contribution comes from the inelastic collisions between the implanted ion and the electronic part of the target system. If S is known as a function of energy, then the total distance travelled by the ion with an initial energy E_0 is

$$R = \int_0^{E_0} \frac{dE}{S(E)}.$$

There is also some lateral deviation of the ion so that the average depth of penetration (so-called projected range) is somewhat less than R.

Since the initial ion energy, typically several tens of keV, is much higher than lattice binding energies (several tens of eV), nuclear collisions may be considered to be elastic (*i.e.*, negligible amount of energy is transferred to the crystal lattice

during such collision). This elastic interaction leads to an angular scattering of the ion and an energy loss by momentum transfer as described by classical kinematics. It is evident that at high speeds of the passing ion the interaction time is short and correspondingly the energy transferred to the host nucleus is insignificant. Therefore the nuclear stopping is important only at relatively low energies of the implanted ions (the maximum occurs at about 1 keV/amu). However, for massive ions (as rare earths) the nuclear stopping may prevail over all the energy range of interest (Fig. 2.3).

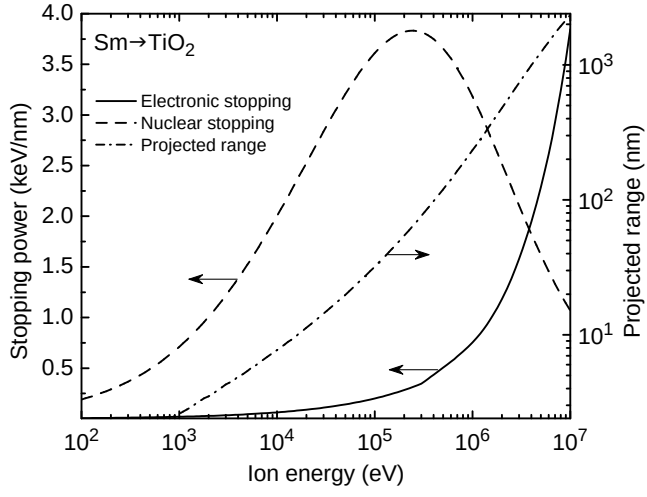

Figure 2.3: Dependence of the stopping power and the projected range of Sm in TiO_2 on the ion energy (SRIM calculation).

A general treatment of the electronic interactions is quite complex. However, in the low energy regime the electronic stopping is analogous to a viscous drag force and is proportional to the ion velocity. Therefore the electronic stopping becomes essential at higher energies. Its maximum is at about 100 keV/amu. The energy loss by incident ion is dissipated through the electron cloud into thermal vibrations of the host matrix. In addition, the interaction is inelastic in the sense that it can lead to the excitation and ionization of the implanted ion itself. At high enough initial energies it is fairly safe to assume that the implanted ion totally looses its identity, so that its initial charge state is of no importance on its final state.

In an amorphous or fine-grained polycrystalline target substance a smooth spatial distribution of implanted ions will evolve. For relatively low energy implantation the distribution is close to a gaussian profile (normal distribution). In higher energy regime the ion distribution may significantly diverge from a gaussian and is frequently much more accurately described by a Pearson IV function, which introduces an asymmetry into the distribution [108, 109]. In the case of RE-implantation into metal-oxides in 10^2 keV energy range the dopant distribution is satisfactorily described by a gaussian profile (Fig. 2.4). However, the final distribution of ions can drastically change with the post-implantation annealing. In a crystalline target channelling effects may modify the impurity profile if the incident ion beam happens to be aligned with a major crystallographic direction.

The ion implantation introduces a large number of point defects (mainly re-

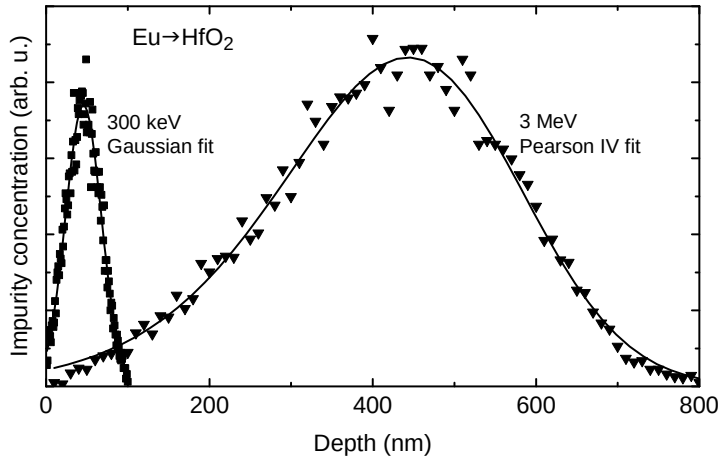

Figure 2.4: Spatial distribution of implanted Eu ions in HfO_2 according to TRIM simulation.

coiled interstitials and corresponding vacancies) orders of magnitude higher than the amount of the dopants. Although the interaction of the ion with the electron cloud of the target can lead to the bond breaking in covalent materials it is usually assumed that the electronic stopping does not contribute significantly to the defect production, at least not in the typical range of energies used [110]. The nuclear stopping is the basic mechanism of defect creation by knocking out the host atoms from their regular lattice positions. These displaced atoms may possess large fractions of the incident ion energy and, in turn, cause cascades of secondary displacements of nearby atoms to form a tree of disorder along the ion path. For heavy ions, experiencing mainly nuclear stopping, the damage can be substantial leading ultimately to a complete amorphisation of the implanted region.

Due to this destructive nature of the implantation process the implanted sample usually requires serious thermal treatment. Thermally stimulated diffusion of atoms within the solid causes the material to progress towards an (energetically favored) equilibrium state which is usually more ordered than the original one. The rate of a temperature activated process (like diffusion, defect relaxation, *etc.*) usually follows the Arhhenius law $\exp(-E/k_{\mathrm{B}}T)$ with E being the activation energy of the process [111]. As in a crystalline material E is usually of the order of 1 eV, one needs quite high temperatures to initiate the processes.

In the course of increasing the temperature one can notice three phases of annealing process: recovery, recrystallization, and grain growth. During the recovery phase the structural defects (produced by *e.g.* ion implantation) as well as the implanted impurity atoms can relax and the latter can form the optical centers. The reduction of structural defects eliminates undesirable charge carrier trapping and recombination centers increasing the yield of luminescence. It is still possible, that certain defects, *e.g.* oxygen vacancies in oxide materials, persist in significant amounts at thermodynamic equilibrium unless the material is annealed

in oxygen-containing atmosphere at high pressures [112]. At high enough annealing temperatures the optical dopants themselves become mobile and redistribute over the sample volume. It is well-known from the diffusion theory that the root-mean-square range of a diffusing entity during a time interval Δt is given by $\sqrt{D\Delta t}$ with D being the diffusion constant. For example, one can roughly estimate that the initial distribution of implanted dopants widens by an amount of $\sim \sqrt{D\Delta t}$. If the solubility of the dopants in the host is low (*i.e.*, the host-quest system is thermodynamically unstable), the long-term heating can lead to the aggregation of impurities and accordingly degradation of luminescence properties. For example, segregation of Er impurities onto surface has been found in GaN [113] whereas precipitation effects prevail in Er:SiO_2 [114] (in both materials the process is stimulated by annealing above 1000 °C). It is frequently found that co-doping with some other impurity can improve the solubility as well as the luminescence properties of the activator.

There exists a freely accessible software package called SRIM aimed for the calculation of the stopping powers and Monte-Carlo simulation of the ion implantation process [115, 116]. This software has been used here for analyzing the rare earth implantation into metal-oxides (Figs. 2.3 and 2.4).

3. INFLUENCE OF WAVEGUIDING STRUCTURE ON THE LUMINESCENCE PROPERTIES OF THIN ALD-GROWN FILMS [I,II]

3.1. Introduction

Since the first demonstrations of cavity effects in the microwave region [117, 118], the possibilities of modifying the characteristics (decay rate, radiation pattern) of a spontaneous emission in the optical regime has been of interest. According to Fermi's Golden Rule the probability of the spontaneous transition of an emitter is proportional to the density of photon states, therefore much attention has been focused on engineering the resonant optical modes around the emitter by placing the emitter either into a metallic cavity, within the distributed Bragg reflectors (DBRs), or into a photonic crystal (for a review, see [119, 120]). The characteristic linear dimension of the cavity must be of the order of wavelength in order to make the photon density significantly different from that of the free space. High Q-factor three-dimensional microcavities, tuned on or off the resonance at transition frequency, enable a complete control over the lifetime and the emitting characteristics of an embedded emitter. Inhibition of spontaneous emission enables to realize, for example, thresholdless lasers. However, a certain degree of control over the emission can be achieved by placing the emitter into a one-dimensional microcavity [121]. The planar cavity actually doesn't enable very significant modification of the decay rate of spontaneous emission. For example, within the ideal planar cavity consisting of two 100%-reflecting metallic mirrors placed half a wavelength apart, the emitter experiences a change of decay rate by a factor of $0.6 \ldots 3.0$ [122]. For DBR cavities the figures are even less pronounced. However, quite dramatic changes can appear in the spectral and directional distribution of the radiation, even in the case of a single dielectric (waveguide-type) layer. In the latter case the most pronounced changes appear in the spectrum of the light leaking out of the film in the limit of total internal reflection [123–129]. The effects associated with planar cavity have found application in *e.g.* the design of LED-s, where one of the most essential challenge is the improvement of the external quantum efficiency (*i.e.* the efficiency of extracting the light from the junction) [130].

In this chapter we are going to outline an investigation of the waveguiding properties of thin anatase films grown by using ALD method. Up to now the atomic layer deposition of titania has been mostly developed for application as high-k dielectric in field-effect transistors in integrated circuits [131]. Their uniform thickness and the possibility to prepare multilayer (laminate) structures also suggest application of the films in optical coatings and waveguiding [132]. However, in the optical regime ALD-grown titania films exhibit usually quite high losses as revealed by transmission spectra [133, 134]. This can be attributed to the nanocrystalline morphology and surface roughness. Yet, it would be interesting to know if the ALD-grown films exhibit any waveguiding ability. The present work was initiated by the observation that the spectral-directional characteristics

of the broadband intrinsic emission of thin crystalline films were significantly modified. Furthermore, as it turned out that the direct measurement of waveguiding using standard techniques was quite complicated due the nature of the films the question arises whether any conclusions on the waveguiding properties of the films can be drawn from the luminescence data.

First we are going to outline a simple theoretical framework (mostly following [130]) for analysis of the subsequent experimental results.

3.2. Overview of the theory of the point-source emission within dielectric layers

In the classical electrodynamics the fundamental laws coverning the behaviour of electromagnetic fields and field-matter interactions are given by the (microscopic) Maxwell equations [135]. In SI system of units these are written as

$$\boldsymbol{\nabla} \cdot \boldsymbol{E} = \frac{\rho}{\varepsilon_0}, \quad \boldsymbol{\nabla} \times \boldsymbol{E} = -\frac{\partial \boldsymbol{B}}{\partial t},$$

$$\boldsymbol{\nabla} \cdot \boldsymbol{B} = 0, \quad \boldsymbol{\nabla} \times \boldsymbol{B} = \mu_0 \boldsymbol{J} + \varepsilon_0 \mu_0 \frac{\partial \boldsymbol{E}}{\partial t}.$$

In a homogeneous dielectric medium the charge density $\rho = 0$ whereas the current density $\boldsymbol{J}$ is non-zero due to the movement of the bound charges: $\boldsymbol{J} = \partial \boldsymbol{P}/\partial t$, where $\boldsymbol{P}$ denotes the polarization of the medium. Considering this one can derive the following wave equation for the electric field:

$$\nabla^2 \boldsymbol{E} - \frac{1}{c^2} \frac{\partial^2 \boldsymbol{E}}{\partial t^2} = \mu_0 \frac{\partial^2 \boldsymbol{P}}{\partial t^2},$$

where $c = (\varepsilon_0 \mu_0)^{-1/2}$ is the speed of light in vacuum. Similar equation can be deduced for the magnetic field strength $\boldsymbol{H}$. The background polarizability is contained in the refractive index n of the medium (*i.e.* $P = \varepsilon_0 \chi E$, $n^2 = 1 + \chi$ with χ being the dielectric permittivity) so that the wave equation takes the form

$$\nabla^2 \boldsymbol{E} - \frac{n^2}{c^2} \frac{\partial^2 \boldsymbol{E}}{\partial t^2} = \mu_0 \frac{\partial^2 \boldsymbol{P}_{\text{sources}}}{\partial t^2}.$$

The right-hand side represents the sources of the electromagnetic field (in the classical sense, accelerated charges, as is evident from the second-order derivative). We are considering the radiation processes at a single frequency ω, so that

$$\boldsymbol{E}(\boldsymbol{r}, t) = \mathrm{Re}\left[\boldsymbol{E}(\boldsymbol{r}) e^{-i\omega t}\right], \quad \boldsymbol{P}(\boldsymbol{r}, t) = \mathrm{Re}\left[\boldsymbol{P}(\boldsymbol{r}) e^{-i\omega t}\right].$$

Here $\boldsymbol{E}(\boldsymbol{r})$ and $\boldsymbol{P}(\boldsymbol{r})$ are the complex amplitudes of the field and the polarization, respectively. After substitution we obtain the time independent wave equation:

$$\nabla^2 \boldsymbol{E}(\boldsymbol{r}) + k_0^2 n^2 \boldsymbol{E}(\boldsymbol{r}) = -\mu_0 \omega^2 \boldsymbol{P}_{\text{sources}}(\boldsymbol{r}), \tag{3.1}$$

where $k_0 = \omega/c$ is the free-space wavenumber. In general there are two kind of sources. The spontaneous emission is a source that is independent of the field at the

source location. In contrast, absorption and stimulated emission are sources that are induced by the local field. In as far that the induced sources are proportional to the field, their effect can be formally accounted for by viewing the refractive index as a complex quantity. Then the imaginary part of the refractive index describes the absorption (or gain) in the medium. In an isotropic medium the components of the vectorial equation (3.1) are uncoupled. Therefore we can hereafter restrict ourselves to the corresponding scalar wave equation

$$\nabla^2\psi(\boldsymbol{r}) + k_0^2 n^2 \psi(\boldsymbol{r}) = \text{sources},$$

where ψ denotes any of the six components of fields $\boldsymbol{E}$ and $\boldsymbol{H}$. In planar layered medium the waves can be classified according to whether the electric field or magnetic field is parallel to the interfaces (*i.e.* perpendicular to the plane of incidence). These solutions are referred to as transverse electric (TE) and transverse magnetic (TM) waves.

Let us consider the emission of an isotropic point source:

$$\nabla^2\psi(\boldsymbol{r}) + k_0^2 n^2 \psi(\boldsymbol{r}) = \delta(\boldsymbol{r}),$$

where $\delta(\boldsymbol{r})$ denotes the 3-dimensional Dirac delta-function. Solution of the equation in an infinite homogeneous medium is the spherical wave

$$\psi(\boldsymbol{r}) = -\frac{1}{4\pi}\frac{\exp(ik_0 nr)}{r}. \tag{3.2}$$

In a layered medium (*e.g.* planar waveguide) we may imagine that the point source still continues to emit the waves given by (3.2). However, due to an interference of the waves reflected and refracted at the interfaces, the radiation pattern seems different to an observer. In order to better analyse the situation it is useful to decompose the spherical wave (3.2) into plane waves of the form

$$\psi_{\boldsymbol{k}} = \exp(i\boldsymbol{k}\boldsymbol{r}).$$

To satisfy sourceless wave equation we require $|\boldsymbol{k}| = nk_0$. Such plane waves form a set of orthogonal eigenfunctions of the sourceless wave equation. Due to the restriction $|\boldsymbol{k}| = nk_0$ we can obtain the plane-wave expansion by two-dimensional Fourier' transform. Let us direct the z-axis perpendicularly to the interfaces so that the refractive index is function of z only. If we choose k_x and k_y as the independent variables in the Fourier' transform, we obtain:

$$\psi(\boldsymbol{r}) = \int_{-\infty}^{\infty}\int_{-\infty}^{\infty} \frac{i}{2(2\pi)^2 k_z} e^{i(k_x x + k_y y + k_z|z|)} dk_x dk_y, \tag{3.3}$$

where $k_z = \sqrt{n^2k_0^2 - k_x^2 - k_y^2}$. As $-\infty < k_x, k_y < \infty$, we see that there are two kind of plane waves. For $n^2k_0^2 - k_x^2 - k_y^2 > 0$ we have propagating waves (k_z real). If $n^2k_0^2 - k_x^2 - k_y^2 < 0$, we have evanescent waves (k_z imaginary). The term $k_z|z|$ in exponent ensures that the evanescent waves are attenuating at large distances from the source. The evanescent waves are required to provide the (spatially) fast oscillations of the wave (3.2) near the point source.

From (3.3) it might not be evident that the plane wave amplitude per unit solid angle is independent of the direction (as expected for an isotropic source). One can see this by rewriting the expansion (3.3) in spherical coordinates (θ, φ):

$$\psi(\boldsymbol{r}) = \left(\int_0^{\pi/2} + \int_{\pi/2+i0}^{\pi/2+i\infty} \right) \int_0^{2\pi} \frac{ink_0}{2(2\pi)^2} e^{i(k_x x + k_y y + k_z |z|)} d\Omega,$$

where $d\Omega = \sin\theta d\theta d\varphi$ is the differential solid angle. The shortcoming of this formulation is that the angle θ becomes complex for evanescent waves. In the present thesis we do not concern about the evanescent part of the field as this remains confined near the waveguide.

Now that we know the plane-wave composition of point-source emission, we can continue the analysis of the point source emission in a layered structure. Consider the plane wave components traveling in directions θ and $\pi - \theta$ with respect to the z-axis (Fig. 3.1). These components have the same (k_x, k_y) but opposite k_z. After each reflection k_z changes its sign and hence the components are coupled. It is easy to see that the amplitude of the resultant upward propagating wave at the plane of the point source is proportional to the following geometric series:

$$\begin{aligned} \psi_{\text{total}} \quad &\propto \quad \left[1 + r_1 r_2 e^{i2\phi} + (r_1 r_2)^2 e^{i4\phi} + \ldots\right] \\ &\quad\; + r_2 e^{i2\phi_2} \left[1 + r_1 r_2 e^{i2\phi} + (r_1 r_2)^2 e^{i4\phi} + \ldots\right] \\ &= \quad \frac{1 + r_2 e^{i2\phi_2}}{1 - r_1 r_2 e^{i2\phi}}, \end{aligned}$$

where r_1, r_2 are the field reflection coefficients from the upper and lower interfaces, respectively, and

$$\begin{aligned} \phi_1 &= nk_0 d_1 \cos\theta, \\ \phi_2 &= nk_0 d_2 \cos\theta, \\ \phi &= \phi_1 + \phi_2 = nk_0 d \cos\theta. \end{aligned}$$

The coefficients r_1 and r_2 are generally complex quantities to account for the possible phase change at reflection.

The relative power flux in direction θ is given by

$$I(\theta) = \frac{\text{Power flux within waveguide}}{\text{Power flux in unconstrained medium}} = \left| \frac{1 + r_2 e^{i2\phi_2}}{1 - r_1 r_2 e^{i2\phi}} \right|^2. \tag{3.4}$$

The essential behavior of this function comes from the Airy factor $1/|1 - r_1 r_2 e^{i2\phi}|^2$ that is well-known from the analysis of the Fabri-Perot interferometry [136]. The Airy factor (as a function of ω or θ) has maxima satisfying the condition

$$2\phi + \Delta\phi = 2\pi m \tag{3.5}$$

with $\Delta\phi = \arg r_1 + \arg r_2$ and m being an integer. These maxima are quite pronounced as $|r_1 r_2| \to 1$ (Fig. 3.2). If one expands the Airy factor to a series

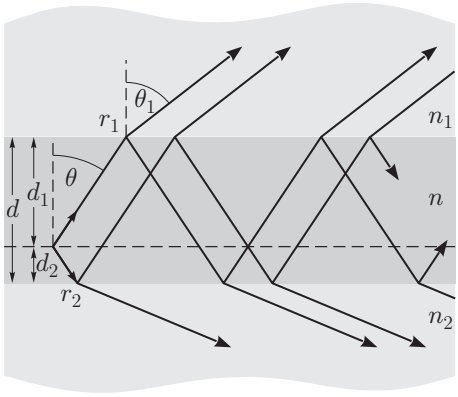

Figure 3.1: Analysis of the point-source emission in a waveguide structure.

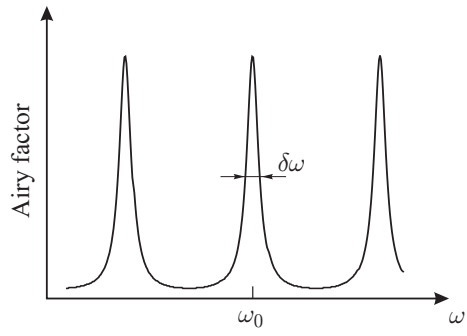

Figure 3.2: Resonance in high-Q cavity.

near a sharp resonance, he will find the lorentzian profile with a full width at half maximum given by

$$\delta\omega = \frac{c(1-|r_1 r_2|)}{nd\cos\theta}. \tag{3.6}$$

For characterizing the quality of resonance one usually introduces the Q-factor:

$$Q = \frac{\omega}{\delta\omega}.$$

As the resonant frequency ω_0 is of the order of $c/nd\cos\theta$, the Q-factor of the planar cavity is of the order of $1/(1-|r_1 r_2|)$.

3.3. Resonance near the total internal reflection

High values of r_1 and r_2 are usually achieved in metallic or DBR cavities. However, high reflectance can be obtained in waveguide-type layers for incident angles near to or exceeding the critical angle of total internal reflection. In the case of a single dielectric interface the $\boldsymbol{E}$-field reflection and transmission coefficients are given by the well-known Fresnel formulae [136]

$$\begin{aligned} r_{\mathrm{TE}} &= \frac{n_\mathrm{i}\cos\theta_\mathrm{i} - n_\mathrm{t}\cos\theta_\mathrm{t}}{n_\mathrm{i}\cos\theta_\mathrm{i} + n_\mathrm{t}\cos\theta_\mathrm{t}} & t_{\mathrm{TE}} &= \frac{2n_\mathrm{i}\cos\theta_\mathrm{i}}{n_\mathrm{i}\cos\theta_\mathrm{i} + n_\mathrm{t}\cos\theta_\mathrm{t}}, \\ r_{\mathrm{TM}} &= \frac{n_\mathrm{t}\cos\theta_\mathrm{i} - n_\mathrm{i}\cos\theta_\mathrm{t}}{n_\mathrm{t}\cos\theta_\mathrm{i} + n_\mathrm{i}\cos\theta_\mathrm{t}} & t_{\mathrm{TM}} &= \frac{2n_\mathrm{i}\cos\theta_\mathrm{i}}{n_\mathrm{t}\cos\theta_\mathrm{i} + n_\mathrm{i}\cos\theta_\mathrm{t}}, \end{aligned} \tag{3.7}$$

where the subscript i refers to the medium containing the incident wave and the subscript t refers to the medium containing the transmitted wave. At angles exceeding the critical angle $\sin^{-1}(n_\mathrm{t}/n_\mathrm{i})$, both r_{TE} and r_{TM} become complex numbers with magnitude 1, *i.e.* total reflection (with a possible phase shift) occurs.

In the waveguide context, the cavity resonances suffering the total internal reflection are called the guided modes, whereas the resonances not experiencing the total reflection are known as the leaky modes [137]. In order to find the externally observed intensity of the leaky-mode emission of an isotropic point source embedded into a planar waveguide (Fig. 3.1), we must improve the expression (3.4) by taking into account the losses and the change of the angular distribution of the plane wave amplitude upon transmission through the interface. The former is given by the Fresnel coefficient t whereas the latter is given by the ratio of the corresponding solid angles:

$$\frac{d\Omega}{d\Omega_1} = \frac{\sin\theta d\theta d\phi}{\sin\theta_1 d\theta_1 d\phi_1} = \frac{n_1^2 \cos\theta_1}{n\sqrt{n^2 - n_1^2 \sin^2\theta_1}}, \tag{3.8}$$

where we have employed the relation $n\sin\theta = n_1 \sin\theta_1$. θ_1 represents the observation angle with respect to the surface normal of the layer. So the final expression for the angular and spectral distribution reads:

$$I(\theta_1, \lambda) = \left| \frac{1 + r_2 e^{i2\phi_2}}{1 - r_1 r_2 e^{i2\phi}} \right|^2 t(\theta)^2 \frac{n_1^4 \cos^2\theta_1}{n^2(n^2 - n_1^2 \sin^2\theta_1)} I_0(\theta, \lambda), \tag{3.9}$$

where $I_0(\theta, \lambda)$ is the emission profile in the unconstrained space.

3.4. Description of samples and experimental details

The thin TiO_2 films studied in this work were grown on amorphous SiO_2 (quartz glass) and single crystal MgO(1 0 0) substrates by employing a chloride-based atomic layer deposition process (see section 2.3 for an overview of the technique). The thickness of the films ranged from 180 nm to 220 nm. The thickness and refractive index were determined from the transmission spectra. According to X-ray diffraction (XRD) and the reflection high-energy electron diffraction (RHEED) studies the films grown on SiO_2 substrates were polycrystalline with preferential (1 1 0) orientation whereby epitaxially grown films were obtained on MgO(1 0 0) substrates. Both samples contained anatase phase. In the latter films, the [1 0 0], [0 1 0] and [0 0 1] directions of anatase were, respectively, parallel to the [0 0 1], [1 0 0] and [0 1 0] directions of MgO substrate. The samples had at least one cleaved (optically smooth) edge that was needed to observe the nearly in-plane PL emission from anatase. A summary of the data on the samples is shown in table 2.

Table 2: Samples used for investigation of leaky-mode emission. T_G denotes growth temperature and $n(E)$ is the refractive index as a function of photon energy (eV).

Label	Substrate	Cycles	T_G (°C)	Thickness (nm)	$n(E)$
233-III	MgO(100)	3000	275	220	$2.484 - 0.018E^2 + 0.0065E^4$
115-III	SiO_2	3000	350	177	$2.426 - 0.026E^2 + 0.007E^4$

The sample grown on MgO substrate was cut into two pieces and one of the pieces was implanted with Sm^{3+} ions accelerated to the energy of 300 keV. The dose of the Sm^{3+} ions applied was $10^{13}\,cm^{-2}$, which led to a quite low average Sm^{3+} concentration of $\sim 2 \times 10^{-3}$ at% in the film. A thermal treatment of the implanted sample was required to observe any Sm-related emission (for a complete description of the annealing process see section 4.3.1).

The PL measurements of the intrinsic emission were carried out in a helium-bath optical cryostat at 5 K. Rare earth emission was studied at room temperature (RT). The PL measurements in the surface normal direction were conducted in the backscattering configuration whereas the nearly in-plane PL was collected in the perpendicular geometry. For a band-to-band excitation of anatase the third harmonic of a Nd:YAG pulsed laser was used (wavelength 355 nm, pulse width ~15 ns). The spectra were recorded with a spectrometer (MDR-23) equipped with a CCD camera (type EEV30-11, produced by Andor Technology). An analyser was used to separate TE- and TM-polarised spectra. The spectra were corrected for the spectral response of the system.

3.5. Results and discussion

In the introductory chapter it was already mentioned that the band-to-band excitation of pure TiO_2 of an anatase phase leads to the formation of self-trapped excitonic (STE) states. The recombination of STE at low temperatures results in a broadband (~0.5 eV) featureless emission spectrum with the intensity maximum at approximately 2.3 eV. In our thin film samples the STE emission is almost totally quenched at temperatures exceeding ~100 K (probably due to the presence of defects introducing non-radiative relaxation routes [32]). Therefore, the intrinsic emission was investigated at 5 K. The spectrum recorded in the direction perpendicular to the film surface is shown in Fig. 3.3(a). The emission was almost unpolarized. The spectrum is quite similar to the emission obtained from high-quality single crystal samples [32, 138]. Subsequently the PL spectrum was recorded in the direction nearly parallel to the film surface (Fig. 3.3(b,c)). For both samples the broadband spectrum was modified into two relatively narrow linearly polarized bands – one of the bands occurred to be TE-polarized (electric vector parallel to the film plane), another one was TM-polarized (electric vector perpendicular to the film plane). The peaks were most pronounced with respect to the unpolarized background signal in the direction tilted about 5° to the substrate side from the exactly in-plane direction as shown in 3.5(a).

The corresponding measurements for Sm^{3+}-doped TiO_2/MgO sample were carried out at RT, because due to the temperature quenching of the STE emission and the enhancement of the Sm^{3+} emission, the latter one dominated at RT (see section 4.3.1). Fig. 3.4(c) presents the unpolarised Sm^{3+} emission series observed perpendicularly to the film surface. At grazing angles the relative intensities of the spectral lines were modified in polarised spectra as shown in 3.4(d). The positions of the maximum and the minimum of polarisation ratio (dashed line) coincided with the polarised peaks determined from the STE spectrum of the same sample. The result confirms that the location and the polarisation of the bands observed at

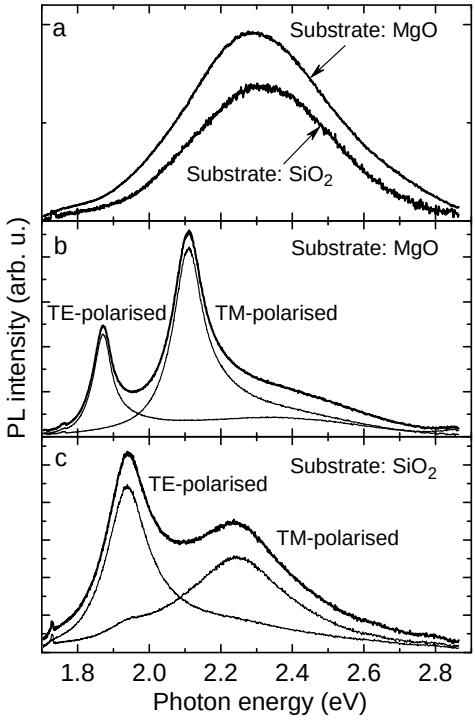

Figure 3.3: PL spectra of the STE emission (at 5 K) of two different TiO_2 samples in the surface normal direction (a) and in the nearly in-plane direction (b,c).

grazing angles is not specific to the emitter but is characteristic of the waveguiding structure.

The experimental arrangement leading to the pronounced spectral narrowing of the STE emission band (Fig. 3.5(a)) suggests that the emission escapes from the sample through the cleaved edge of the substrate. Considering the anatase film as an asymmetric slab waveguide, we are observing the cavity effect in the limit of the total internal reflection (Fig. 3.5(b)). At the critical angle of total reflection ($\sin\theta = n_s/n$, with n_s denoting the refractive index of the substrate) the resonance condition (3.5) reduces to

$$\frac{4\pi d\sqrt{n^2 - n_s^2}}{\lambda} + \Delta\phi = 2\pi m. \tag{3.10}$$

The thickness and refractive index of the films have been obtained from transmission spectra (table 2). The order of interference corresponding to the observed modes turned out to be $m = 1$. By using these data the numerical solution of Eqn. (3.10) gives the following peak positions that quite satisfactorily correlate to the experimentally observed ones:

Sample	Observed (eV)		Calc. (eV)	
	TE	TM	TE	TM
TiO_2/MgO	1.87	2.11	1.88	2.17
TiO_2/SiO_2	1.94	2.25	2.07	2.41

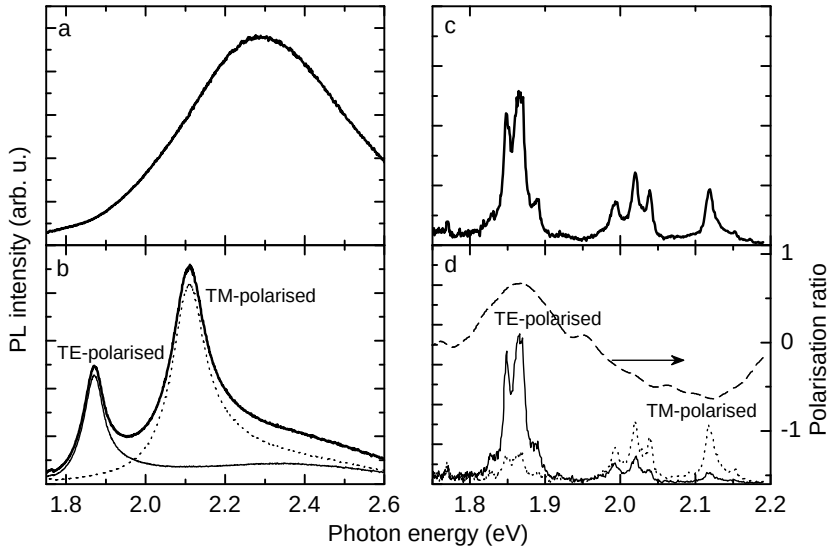

Figure 3.4: Dependence of the PL spectra of the STE and the impurity (Sm^{3+}) emission on the observation direction. (a) STE emission from pure anatase film recorded in the surface normal direction and (b) in the nearly in-plane direction at 5 K; (c) Sm^{3+} emission from implanted sample recorded in the surface normal direction and (d) in the nearly in-plane direction at RT.

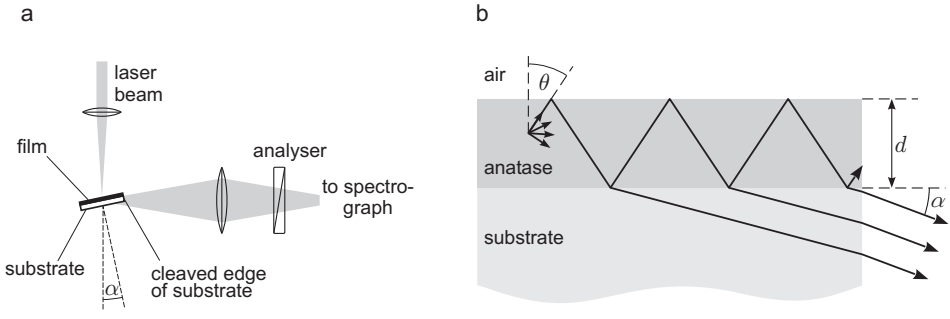

Figure 3.5: (a) Experimental arrangement for observation of nearly in-plane PL; (b) Propagation of the PL emission escaping from the sample through the cleaved edge of the substrate.

Yet, some discrepancy between the experimental and theoretical values is evident. In the case of TiO_2/MgO the minor differences can have several origins. Most probably, this is related to the birefringence of the anatase crystal with $n = 2.51$ for $\boldsymbol{E}$ parallel to the optic axis and $n = 2.57$ for $\boldsymbol{E}$ perpendicular to the optic axis [50]. The XRD and RHEED measurements have revealed that in our anatase films grown on MgO substrate the in-plane orientation of the optical

axis of crystallites is allowed in two mutually perpendicular directions [41]. This suggests that the effective optical medium has an optical axis perpendicular to the film plane and, correspondingly, the refractive index is different for TE- and TM-polarised beams. This anisotropy is not revealed for the light wave, which has the electric vector parallel to the film surface. In the case of TiO_2/SiO_2 the discrepancy between the experimental and theoretical values is more significant and presently no satisfactory explanation can be given.

The accuracy of the present investigation does not allow a full quantitative comparison to Eqn. (3.9). Yet, it can be shown that the results qualitatively agree with Eqn. (3.9). First of all, we note that the TM-polarized emission is spectrally somewhat broader than the TE-polarized one. This can be attributed to the behavior of the amplitude reflection coefficient r_1 near the critical angle. If we consider $|r_1|$ as a function of the observation angle α (Fig. 3.5(b)) and expand the Fresnel formulae (3.7) at $\alpha = 0$ up to the linear term, we obtain

$$|r_1(\alpha)| \approx 1 - \frac{2\gamma\alpha}{\sqrt{n^2 - n_s^2}},$$

where $\gamma = 1$ for TE-polarization and $\gamma = n^2/n_s^2$ for TM-polarization. We can see that $|r_1(\alpha)|$ falls off more rapidly for TM-polarization, which explains the difference in mode widths (for $\alpha \sim 5^\circ$). The numerical estimates of the widths (according to (3.6)) are also in agreement width the experiment. In addition, owing to the factor (3.8), Eqn. (3.9) predicts that the intensity of leaky-mode emission falls to zero for $\alpha \to 0$. This explains the most pronounced appearance of the spectrally narrowed emission at an angle different from zero ($\alpha \sim 5^\circ$).

Finally we note that the spectral narrowing of the nearly in-plane emission can also be described in the context of cavity quantum electrodynamics (CQED) although specific CQED effects are not revealed in our experiments. The film could be considered as a planar optical cavity for that part of the emission that suffers a total internal reflection at the interfaces. For that part of the emission the component of the wave vector that is parallel to the surface normal is quantized due to a cavity effect. This will also lead to the quantization of the wavelength of the light that is observed in the limit of the total internal reflection. A full analysis of the problem in the context of CQED would require evaluation of electromagnetic field mode density (*i.e.* density of states) and application of Fermi's Golden Rule for the rate of spontaneous emission. The calculation is not carried out here as a result similar to the classical expression (Eqn. 3.4) is expected.

3.6. Conclusion

The investigations have clearly demonstrated that atomic-layer-deposited thin films possess waveguiding effect. Unfortunately, the present study did not enable quantitatively estimate the waveguide losses. Such measurements would require more sophisticated experimental setup. Application of *e.g.* m-line spectroscopy for the investigation of the waveguiding properties has turned out to be quite complicated probably due to the surface roughness of the films. Both AFM as well as ellipsometric studies have indicated a surface roughness of the order of 10 nm.

The observed widths of the leaky-mode resonances were not significantly reduced when smaller collecting angles were used. Therefore it seems that instead of the non-unity reflection some other mechanism makes essential contribution to the mode width. Most probably this might be a scattering at crystallite interfaces and/or rough film surfaces. The reduction of waveguiding ability due to scattering at nanocrystallite interfaces is a well-known problem, arising *e.g.* of crystallization of sol-gel layers during high-temperature thermal treatment [78]. By a suitable choice of growth conditions (mainly substrate temperature) the ALD process can be employed for preparing amorphous films [133]. However, if one is interested in the optical activation through the impurity doping and optical excitation of the impurities via energy transfer from the host material, the crystalline matrices might have better performance. Amorphous environment also leads to a significant broadening of RE resonances which is unfavorable for a laser operation. Hopefully the advancements in the growth technique will allow preparation of waveguiding layers applicable in photonics.

From the fundamental aspect the investigation has once again shown that a dielectric waveguide significantly modifies the spectral-directional characteristics of an emitter inside the film with the most remarkable changes taking place for the emission observed in the direction nearly parallel to the film plane. Such effects are most easily observable for a broadband emission. As the positions of the polarised peaks at grazing angles are quite sensitive to the film thickness and to the refractive index in the excited spot of sample, the effect could be applied as an alternative method for obtaining the optogeometric parameters and to characterize the homogeneity of thin films (*i.e.*, estimate the refractive index and thickness variations).

4. LUMINESCENT MATERIALS BASED ON RE-ACTIVATED METAL-OXIDES [III–VIII]

4.1. Introduction

Several papers report on the optical activity of REs in metal-oxides TiO_2, ZrO_2, and HfO_2. Energy transfer from host to Sm^{3+}, Eu^{3+}, Yb^{3+}, Nd^{3+}, and Er^{3+} ions in sol-gel-prepared TiO_2 under a band-to-band optical excitation has been reported by several authors [77, 81]. It is suggested that the energy transfer takes place through a defect level of TiO_2 so that the energy of this level must exceed the energy of the lowest emitting level of RE^{3+} in order for the energy transfer to occur. For example, Tb and Tm do not excite via energy transfer. However, the PL spectra presented usually lack any fine structure indicating essential contribution of amorphous phase or nanocrystallite interfaces. Eu^{3+}-, Tb^{3+}-, and Sm^{3+}-doped zirconia were prepared via sol-gel-route by Reisfeld et al. [76]. It was shown that expectedly (due to lower phonon frequencies) the PL intensity was more pronounced in the case of zirconia as compared to similar silica samples. Yet, there was no observation of energy transfer and the fine structure of the PL spectra was unresolved. Quite detailed investigation of PL emission and energy transfer of Sm^{3+} in monoclinic ZrO_2 has been conducted by different research groups [82, 139, 140]. There seems to exist some ambiguity in the correct assignment of electronic transitions to the observed emission lines. Villanueva-Ibañez et. al. has studied Eu^{3+}- and Tb^{3+}-doped sol-gel-prepared HfO_2 powders aimed for scintillating applications [80]. There are several reports on the use of Eu^{3+} emission as a structural probe for observation of ZrO_2 phase transitions [141, 142]. To our knowledge the Sm^{3+} emission has not been observed in HfO_2 matrices. The sol-gel method is evidently the most widely used method for preparing the materials for optical and luminescence applications.

In the present work the RE-doped TiO_2, ZrO_2, and HfO_2 materials were obtained via two different routes – the atomic layer deposition (ALD) followed by ion implantation and the sol-gel method. The main emphasis is on the former method which generally enables more reliable and controllable preparation of thin film materials. Investigation of ALD-grown samples is also of special interest as this method has not been so widely employed for preparation of optical materials. Yet, sol-gel method has been developed primarily due to the possibility of *in situ* doping and to obtain nanoporous materials which exhibit some very interesting gas sensing behavior described later in this chapter.

4.2. Description of samples and experimental details

4.2.1. ALD-grown samples

Thin films were grown by using chloride-based ALD processes. The films were deposited on single-crystal (1 0 0)-oriented Si substrates in the low-pressure ALD

reactor.[5] The precursors were alternately led to the substrate by using N_2 as the carrier gas. After each precursor pulse the reactor was purged by pure N_2. The lengths of the precursor exposure times and the purge periods between precursor pulses were kept constant at 2 s. The other process parameters, the phase content of the as-grown films (as determined by the XRD and the RHEED methods) as well as the thicknesses and refractive indices (as estimated from reflection spectra) are shown in table 3. Unfortunately the ALD method did not allow the growing of phase-pure monoclinic ZrO_2 films. The details of the ALD processes employed have been described in [90, 98, 99].

Table 3: ALD-samples used for PL investigation. T_G is the growth temperature in °C, d is the thickness in nm and n is the refractive index at 580 nm. The final column displays the average number of impurity ions per formula unit of host material (at%).

Label	Content	T_G	Cycles	Phase	d	n	Concentr.
89-IV	TiO_2:Sm	275	3000	anatase	230	2.37	1.5×10^{-3}
639-IV	HfO_2:Sm	750	2400	monoclinic	180	2.04	1.9×10^{-3}
446-II	ZrO_2:Sm	300	2000	tetrag./monocl.	250	2.1	1.4×10^{-3}
589-V	TiO_2:Eu	325	1500	anatase	100	2.4	0.040
1244-IV	HfO_2:Eu	600	1500	monoclinic	130	2.05	0.030
1240-III	ZrO_2:Eu	300	1000	tetragonal	120	2.15	0.034

The doping of ALD-grown samples was achieved by an implantation with Sm^{3+} and Eu^+ ions at room temperature. 300 keV ion energy was chosen as this results in a projected range at approximately in the middle of the film (by SRIM calculation, see Fig. 2.3). For Sm^{3+} ions the total dose applied was $10^{13}\,cm^{-2}$, whereas for Eu^+ ions it was $1.14 \times 10^{14}\,cm^{-2}$. According to TRIM simulation, the 300 keV energy results in a gaussian-shaped concentration distribution of ions having a width of about 60 nm as shown in Fig. 2.4. The estimated impurity concentration averaged over the film thickness is shown in table 3.

An annealing of the as-implanted samples was needed to observe any emission of incorporated RE ions. The annealing in air (at normal pressure) was performed at the temperatures ranging from 300 °C to 1100 °C in the steps of 100 °C, for 15 min at each applied temperature. The influence of this treatment to PL properties is described in section 4.3.1.

Spectroscopic ellipsometry was used to examine the influence of ion implantation on the optogeometric parameters of the HfO_2:Eu sample. A single-layer analysis of the data shows that the as-grown film was 117 nm thick, the refractive index being 2.00 (at 500 nm). The corresponding values for the implanted film (prior to annealing) were 121 nm and 2.03. Double-layer analysis showed that there was a thin (∼10–15 nm) layer of a very low refractive index on top of the film.

[5] The silicon substrates were chosen because these do not contribute to the photoluminescence emission even in the UV range.

This layer is interpreted as an effective medium arising of the surface roughness. In the case of implanted film the layer was thicker and of lower refractive index.

4.2.2. Sol-gel-prepared samples

Sol-gel technique was applied for preparing nanosized films and powders of TiO_2. Proper metal-oxide sol precursors were obtained by adding 1.8 g solution containing water, concentrated HCl and n-buthanol (mole ratio 1:0.03:13) to the 0.5 g $Ti(OBu)_4$ and the mixture was stirred for 1 h at 21 °C. For doping with Sm, 1% of $SmCl_3 \cdot 6\,H_2O$ was dissolved into the mixture of water and buthanol.

For preparation of films 12.5 g of hexane was added to the solution in order to slow down the polymerization reaction of $Ti(OBu)_4$. The films were deposited onto high-quality quartz substrates, which were cleaned with acetone and heated for 2 min at 200 °C prior to deposition. The Sm concentration in the resulting films was estimated to be ∼0.1 at%. The films were baked between every coating-cycle for 1 min at 200 °C. To release the traces of organic compounds and to crystallize the films, the final thermal treatment was carried out for 2 h at 520 °C in the air. The thicknesses of the films, as obtained from ellipsometrical measurements, ranged from 3 nm up to 50 nm, with an increase of 3 nm per growth cycle. The refractive indices ($n \sim 2.25$) indicated noticeable porosity in thicker films. AFM images indicated the presence of nanocrystals of ∼20 nm size on surface of the films.

For preparation of powders n-buthanol was removed by rotator evaporator at 70 °C and 8 torr during 15 min. Subsequently 2.3 g of hexane was added to the residue. Obtained precursor was added dropwise to stirred distilled water at 70 °C. Powder was obtained by drying the colloidal solution at 100 °C. The final thermal treatment of the powders was carried out for 15 min at 700 °C in the air. Raman-scattering studies indicated an anatase phase and the width of the raman peaks showed a particle size of about 10 nm in the obtained powders.

4.2.3. Experimental

Most PL measurements were performed at room temperature (RT) in backscattering configuration. In addition, a He-bath optical cryostat was used for conducting laser-stimulated PL measurements in the temperature range of 5...300 K. For a band-to-band excitation of TiO_2 the third harmonic of a Nd:YAG pulsed laser was used (wavelength 355 nm, pulse width ∼15 ns). The operation frequency of the laser was either 5 kHz or 500 Hz depending on whether the PL spectrum or the PL decay was measured. Frequencies lower than 500 Hz could not be achieved with this laser, thus limiting the maximum observable range of PL decay kinetics to 2 ms. The energy density of excitation was of the order of $0.5\,\mu J/mm^2$. PL of ZrO_2 and HfO_2 was excited by using a pulsed ArF excimer laser (wavelength 193 nm, pulse duration 10 ns, frequency 30 Hz) or a synchrotron radiation with the photon energy tunable in the range of 4...20 eV. The energy density of excitation achieved by the ArF laser was about $0.5\,mJ/mm^2$. The measurements with synchrotron radiation were carried out in an ultra-high vacuum ($\sim 10^{-9}$ mbar) by using a Utrecks-type He-flow cryostat to achieve low temperatures (10 K). The

synchrotron radiation is pulsed with pulse separation of 192 ns and pulse width of 130 ps. The spectral width of the synchrotron radiation was 0.2 nm and the average power of the order of 0.1 μW. The excitation spectra obtained by means of synchrotron radiation were corrected using the excitation spectrum of Na-salycilate as a reference (in the spectral range studied the luminescence yield of Na-salycilate is known to be independent of the excitation energy). For a direct excitation of Sm^{3+} a pulsed GaN laser diode module emitting at 402 nm was used (100 kHz, 250 μW).

The laser-stimulated emission spectra were recorded by using a spectrograph (MDR-23) equipped with an ICCD detector (Andor Technology, model DH501-16F-03), that permitted time-resolved measurements with as high resolution as 5 ns. In some cases it was also favorable to use the camera for recording the PL decay kinetics. All spectra were corrected for the spectral response of the system. Decay kinetics of RE emission was recorded by using a photon counting system consisting of a Hamamatsu photomultiplier tube (model H8259-01) and a FAST ComTec multichannel analyser (model P7882, resolution 100 ns). Emission excited by synchrotron radiation was recorded by using an ARC SpectraPro-308 monochromator-spectrograph equipped with either a liquid nitrogen-cooled CCD detector (Princeton Instruments) or a Hamamatsu R6358P photomultiplier tube.

The investigation of the influence of the ambient gas on the photoluminescence was conducted in an optical chamber that could be evacuated down to 0.1 torr in a few seconds. The sol-gel-derived powders were fixed by placing them into a small ($5 \times 5\,mm^2$) nickel grid with a grid size of $\sim$50 μm.

4.3. Results and discussion

4.3.1. Photoluminescence spectra

Under a band-to-band optical excitation all the RE-doped materials emitted a luminescence characteristic to the RE ions in trivalent charge state (Figs. 4.1 and 4.2). The fine structure arises due to the splitting of spinn-orbitals in the crystal field. The well-resolved Stark components indicate that the RE ions occupy a few well-defined lattice sites. The fine structure of RE^{3+} emission is almost identical in ZrO_2 and HfO_2, but markedly different from that of RE^{3+}:TiO_2. The almost exact correspondence between the Stark components in ZrO_2 and HfO_2 indicates that in these matrices the RE ions experience a similar local environment. Also, no significant differencies were found in the Sm^{3+} spectra of ALD-grown and sol-gel-derived TiO_2. In the case of TiO_2 powders it was also possible to observe direct excitation of Sm^{3+} at 402 nm due to the larger amount of material present.[6] The PL spectra as well as the excitation efficiencies were quite similar for direct and indirect excitation.

The visible luminescence of Sm^{3+} ion is usually composed of four well-separated emission bands that are assigned to the transitions from the lowest excited level

[6]There is a possibility that actually an indirect excitation takes place via the band tails at room temperature. Measurements at lower temperatures would clarify this issue as the band gap of TiO_2 increases with decreasing the temperature.

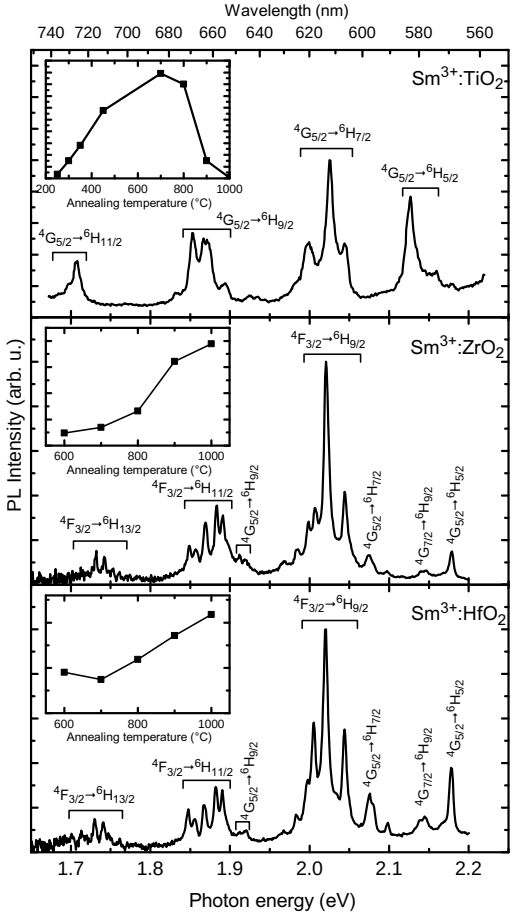

Figure 4.1: Sm^{3+} PL spectra in metal-oxide matrices. The spectral resolution is 0.5 nm ($\sim$ 2 meV). The inset shows the dependence of the PL intensity on the annealing temperature.

$^4G_{5/2}$ to the various ^6H_J levels (Fig. 4.3). This is valid if the excitation is relaxed to the $^4G_{5/2}$ level. If this is not the case more complicated emission patterns can arise as the lowest excited Sm^{3+} levels $^4G_{5/2}$, $^4F_{3/2}$ and $^4G_{7/2}$ as well as the ^6H_J levels are almost equally spaced. A PL spectrum of ZrO_2:Sm^{3+} with a fine structure quite close to our results has been reported by Assefa et al. who have assigned the emission to the transitions from the three above-mentioned excited states as shown in Fig. 4.1 [140]. However, the time-resolved measurement of the Sm^{3+} emission in our samples indicates that the decay rate is equal for all transitions in the spectral range studied. For example, all emission lines were present when recorded in the time window 1–10 ms after excitation, therefore none of the emission lines experiences a fast relaxation. This seems to support the conclusion that the emission follows from a single initial state. However, it might be that the decay rate is mainly determined by the rate of RE excitation by slowly migrating charge carriers as also suggested by the decay curves (see next section) rather than by the radiative decay. In that case the fast and slow transitions might

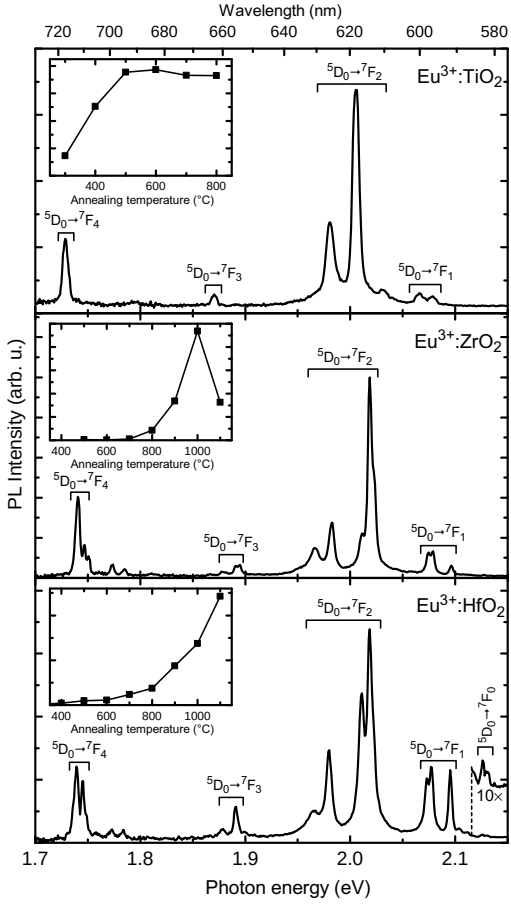

Figure 4.2: Eu^{3+} PL spectra in metal-oxide matrices. The spectrum of Eu^{3+}:HfO_2 corresponds to annealing temperature of 1100 °C whereas that of Eu^{3+}:ZrO_2 corresponds to 1000 °C in which case the PL intensity was highest. The spectral resolution is 0.5 nm (∼2 meV). The inset shows the dependence of the PL intensity on the annealing temperature.

not be well separable.

In the case of Eu^{3+} the assignment of transitions is more straightforward as all the observed transitions originate from the single level $^5D_0$. This is confirmed by the time-resolved measurements. Yet, in the higher-energy spectral range a bunch of sharp lines were found (not shown in Fig. 4.2) with a decay time in μs range indicating that the emission follows from higher excited states (mainly $^5D_1$) that are being rapidly depopulated.

Dependence of photoluminescence on annealing temperature was studied. The emission intensity of Eu^{3+} in TiO_2 saturates after annealing at 600 °C (Fig. 4.2). Sm^{3+} emission in TiO_2 was maximized upon annealing at 700 °C and shows a rapid quenching thereafter (Fig. 4.1). This behavior might be related to the phase transition to the rutile form at these temperatures (confirmed by Raman-scattering measurements). Possibly the energy transfer from TiO_2 host to Sm^{3+} does not work in the rutile polymorph. The direct excitation of Sm^{3+} in TiO_2 powders was also impossible after annealing at 1000 °C. Band-to-band excitation of nanopowders at this annealing reveals a very weak and significantly deformed PL spectrum

of Sm^{3+}. Therefore these Sm^{3+} ions must be located in a different environment in accordance with the phase transformation. Another possible explanation of PL degradation is the segregation of ions onto surface or precipitation. However, if some kind of agglomeration of impurities is responsible for the luminescence quenching, it follows that the solubility of the RE atoms is extremely low in TiO_2 considering the initial concentration achieved by ion implantation (Table 3).

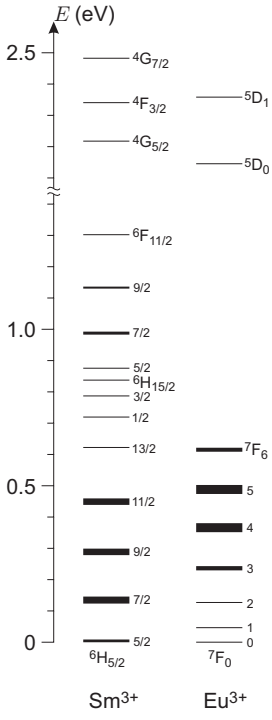

Figure 4.3: Portion of the "Dieke diagram" showing energy levels of the Sm^{3+} and Eu^{3+} ions (note the break of the energy axis). The width of the levels characterizes the amount of splitting experienced in a crystalline environment.

The RE^{3+} emission in ZrO_2 and HfO_2 shows improvement up to the highest annealing temperatures used (Figs. 4.1 and 4.2). The exceptionally strong emission of Eu^{3+}:ZrO_2 after annealing at 1000 °C is actually due to the amplification of the ${}^5D_0 \rightarrow {}^7F_2$ transition as indicated by the PL spectra. Decay curves (see next section) indicate that fast decay components that were normally present at other annealing temperatures have also disappeared. No explanation of these effects can be given at present.

Eu^{3+} ion is known to be a good optical probe of local environment. First of all the number of different Eu^{3+} emission centers is usually determined by the number of non-split ${}^5D_0 \rightarrow {}^7F_0$ emission lines [143]. In the present case the weak emission lines at 582 nm in the PL spectrum of Eu^{3+}:HfO_2 can be tentatively attributed to ${}^5D_0 \rightarrow {}^7F_0$ transition (Fig. 4.2). It follows then that at least two different lattice sites exist for Eu^{3+} ion. As Eu^{3+} and Sm^{3+} are quite similar by the ionic radius and the outer shell configuration, the same conclusion should be applicable for Sm^{3+} centers. In TiO_2 these emission lines could not be detected. They were also too weak in ZrO_2 to draw any reliable conclusion.

In spite of the possible mixing of the emissions of different centers we summarize here the group-theoretical results for the simplest case if the emitting ion occupies the regular substitutional position in the crystal lattice and if the emission originates from a single excited level of negligible splitting. Sm^{3+} is a RE ion containing an odd number of electrons (half-integer J). The analysis shows that when situated into a noncubic crystal field, the free-ion energy level with the total angular momentum quantum number J splits into $J + 1/2$ doubly degenerate Stark components (Kramers degeneracy is maintained) [57]. In the case of Eu^{3+} the results are slightly more involved depending on the exact point symmetry of

Table 4: Symmetry properties of substitutional impurity sites [141, 145].

	TiO_2		ZrO_2, HfO_2		
	Rutile	Anatase	Monocl.	Tetrag.	Cubic
Coord. number	6	6	7	8	8
Local symmetry	D_{2h}	D_{2d}	C_s	D_{4d}	O_h

the emission center. Assuming that the ion occupies the position of the metal ion without a remarkable deformation of the neighboring environment the symmetry point groups shown in Table 4 are applicable. In the local field of D_{2d} symmetry the spin-orbitals $^7F_4$, $^7F_3$, $^7F_2$, and $^7F_1$ are split to 7, 5, 4, and 2 levels, respectively. The corresponding numbers of sublevels in the C_s symmetry are 9, 7, 5, and 3. The results are generally in accordance with the fine structure in the spectra in Figs. 4.1 and 4.2. In some cases the number of observable emission lines is less than predicted probably because of the weakness and/or partial overlapping of the transitions due to homogeneous (at room temperature) or inhomogeneous broadening. It is also possible that the relatively large size of the RE ions enforces an approximately cubic local environment as suggested in the case of Sm^{3+}:$BaTiO_3$ [144]. In the present case the observed number of Stark resonances exceeds that expected for a cubic crystal field. This supports the proposition that there exists at least two different lattice sites for RE impurities.

As a second symmetry-probing feature of Eu^{3+}, it is well-established that the $^5D_0 \rightarrow {}^7F_1$ transition is of magnetic dipole nature whereas the $^5D_0 \rightarrow {}^7F_2$ transition is of a forced electric dipole origin. The former is quite insensitive to the site symmetry whereas the latter is pronounced if the ion is located in a low-symmetry site lacking the inversion symmetry [60]. Therefore the ratio of intensities of $^5D_0 \rightarrow {}^7F_2$ and $^5D_0 \rightarrow {}^7F_1$ transitions (we will call it e/m-ratio for short) is highly sensitive to the symmetry of the local environment. Application of this property of Eu^{3+} ion as a structural probe has been demonstrated in several works [85, 87, 141, 142, 146]. In the metal-oxides studied here the local environment of substitutional Eu^{3+} reflects also the crystalline phase (Table 4). It has been proposed that the e/m-ratio acquires the values 2.81, 1.65, and 1.62 in the monoclinic, Ca^{2+}-stabilized tetragonal, and Ca^{2+}-stabilized cubic phase of ZrO_2, respectively [142]. In the present case the ratio for ZrO_2 depended on the annealing temperature approaching a value of 2.8 as shown in Fig. 4.4. This can be attributed to the formation of monoclinic surrounding for Eu^{3+}. After annealing at 1000 °C there was a boost of the e/m-ratio. The overall PL intensity of Eu^{3+} was also highest at this point. Possibly the annealing at 1000 °C favors the formation of monoclinic phase of ZrO_2. In the case of HfO_2 the annealing-dependence of the e/m-ratio was relatively less-pronounced. For some reason, there was a drop of the value at 1000 °C.

In connection to the possible role in the energy transfer from host to guest it is of interest to study the changes in the intrinsic emission induced by the doping of the materials. At low temperatures the broadband emission of TiO_2:Sm^{3+} was

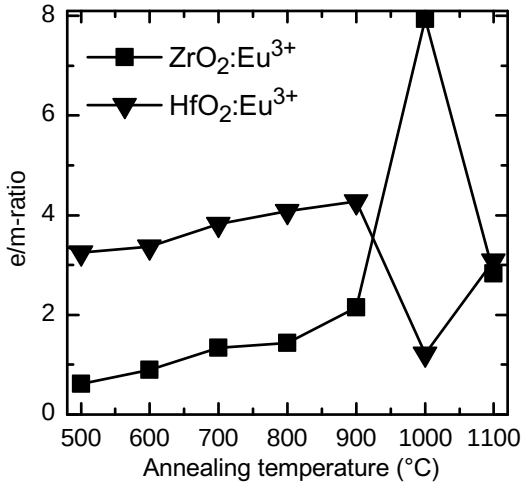

Figure 4.4: Dependence of the ratio of the intensities of ${}^5D_0 \rightarrow {}^7F_2$ and ${}^5D_0 \rightarrow {}^7F_1$ transitions of Eu^{3+} ion on the annealing temperature.

studied.[7] The low-temperature PL spectra of TiO_2:Sm^{3+} consist of a broadband emission superposed by the Sm^{3+} emission lines (Fig. 4.5a). The broadband emission is spectrally substantially broadened as compared to the emission spectrum of an undoped film (0.75 eV vs. 0.45 eV). Also, the temperature quenching of the broadband emission of doped films proceeds significantly slower than in undoped samples (Fig. 4.6).

In the undoped ALD samples the broadband emission is most probably of self-trapped excitonic (STE) origin. The well-defined nature of this emission follows from the elementary gaussian shape of the band. Yet, comparison to the available data about the similar emission band in pure anatase single crystal [32] shows that the emission in our films is a bit spectrally narrower and quenches significantly faster with increase of temperature (Fig. 4.6). Therefore the self-trapping is probably assisted by the presence of some specific kind of defects.

The broadband emission of doped samples seems to contain several contributions. At low temperatures the main emission is around 2.2 eV. At room temperature the emission is mostly quenched but a spectrally very broad background remains. The decay of the emission centered at 2.2 eV follows asymptotically a power-law $I(t) \propto t^{-m}$ with $m = 0.95$ in ALD-grown sample and $m = 1.1$ in sol-gel-derived sample (Fig. 4.5(b)). This behavior is similar to that of the STE emission of anatase single crystal [35, 36] and is attributed to a tunnelling recombination of randomly distributed electrons and holes. In conclusion, apart from the broadened spectrum the emission behaves quite similarly to the STE emission. The broadening is very likely inhomogeneous owing to the presence of a distribution of defect centers which assist the formation of the relaxed excitonic state. The role of Sm^{3+} ions themselves in these processes is questionable due to their low concentration. Therefore at least in implanted sample we can consider Sm^{3+} as simply a probe of photoexcited charge carrier dynamics.

[7] The broadband emissions of ZrO_2 and HfO_2 samples showed quite complex behavior which is not considered in this work.

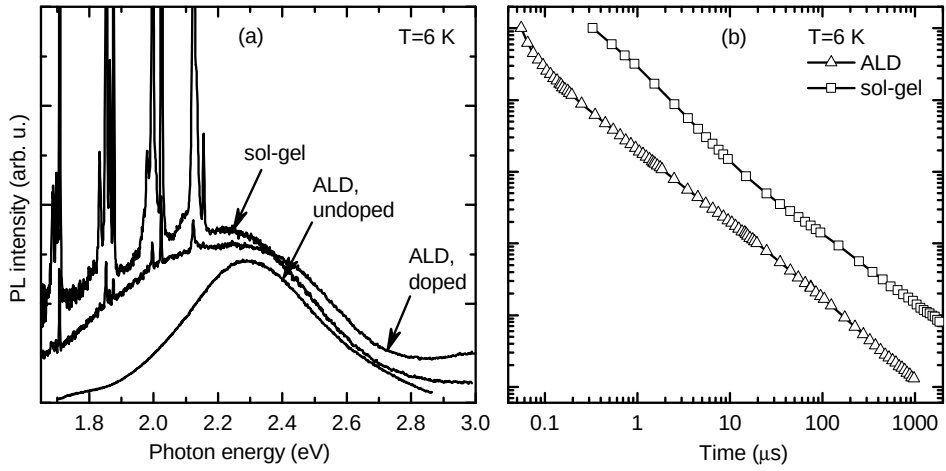

Figure 4.5: (a) Low-temperature emission spectra of TiO_2:Sm^{3+} samples in comparison to the that of an undoped nanocrystalline anatase film. The emission is excited at 3.49 eV. The Sm^{3+} emission is stronger in sol-gel-derived sample due to the higher concentration of the ions. (b) The decay curves of the broadband emissions shown in part (a). The curves have been shifted for clarity.

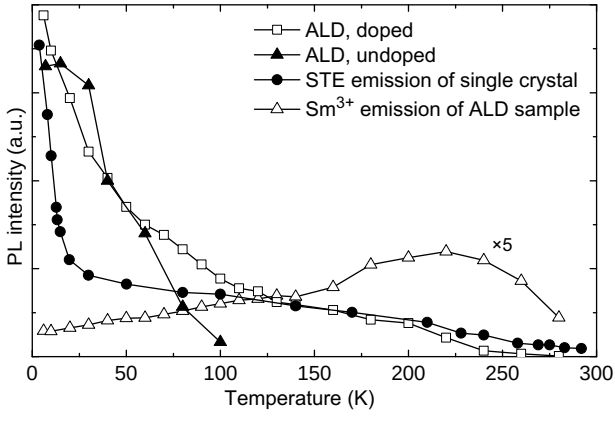

Figure 4.6: Temperature-dependence of the broadband emission of pure and Sm^{3+}-doped TiO_2. Data on STE emission in single crystal is according to [32].

4.3.2. Photoluminescence decay

One can employ the PL decay kinetics as a supplementary indicator of the crystal recovery upon annealing. Figure 4.7 shows the PL decay kinetics in dependence on the thermal treatment. The decay kinetics is essentially non-exponential for all materials studied but approaches a single exponential function at highest annealing temperatures. The prevalent decay times present in the kinetics are shown in table 5. Expectedly, ZrO_2 and HfO_2 exhibit similar behavior. In TiO_2 the decay times are significantly smaller.

Yet, it might seem peculiar that the decay kinetics is not satisfactorily single-

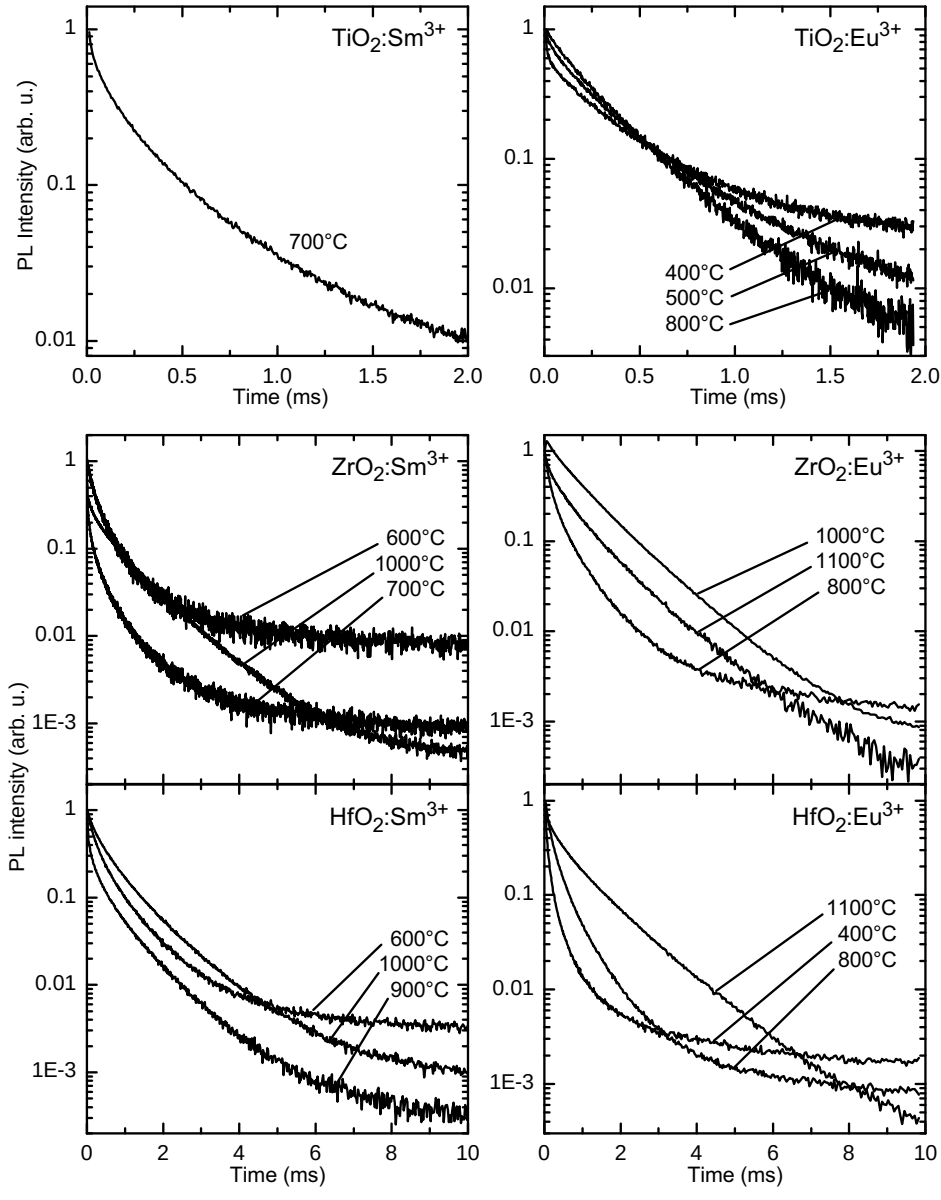

Figure 4.7: Decay of RE^{3+} emission in TiO_2, ZrO_2, and HfO_2 in dependence on the annealing temperature.

Table 5: RE^{3+} PL decay times in the metal-oxides studied.

Emitter	Annealing	Decay time
Sm^{3+}:TiO_2	15 min/700 °C	~600 μs
Sm^{3+}:ZrO_2	15 min/1000 °C	1.15 ms
Sm^{3+}:HfO_2	15 min/1000 °C	1.28 ms
Eu^{3+}:TiO_2	15 min/800 °C	348 μs
Eu^{3+}:ZrO_2	15 min/1100 °C	1.28 ms
Eu^{3+}:HfO_2	15 min/1100 °C	1.30 ms

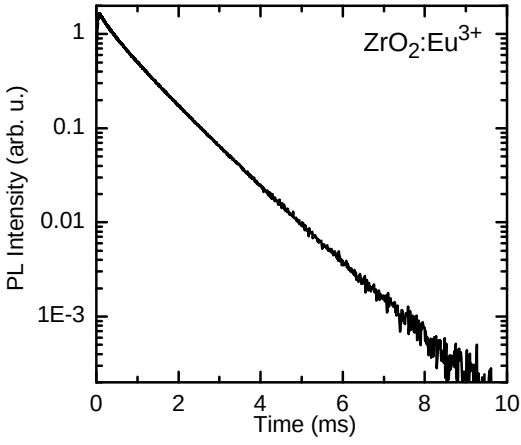

Figure 4.8: Decay of Eu^{3+} emission in ZrO_2 (annealed at 1100 °C) when excited at lower intensity.

exponential even after annealing at 1100 °C. More careful measurements revealed that the behavior depends on the intensity of excitation. At somewhat lower excitation energy densities is was possible to record almost single-exponential decay, as depicted for Eu^{3+}:ZrO_2 in Fig. 4.8. The lifetime is 1.08 ms. The non-exponential decay at moderate annealing treatments can be attributed to the following mechanisms. First of all, we note that there exists decay components much faster as well as much slower than the normal lifetime approached at highest annealing temperatures. The fast decay components can be attributed to the quenching of RE excitation via nonradiative channels, *e.g.* an energy transfer to the defects surrounding the RE ion. Such quenching is observed in *e.g.* Er^{3+}:GaN [147]. Indifferently to that work the initial parts of the decay curves observed in our case cannot be satisfactorily fitted by assuming a single type of defects responsible for the quenching (in that case a decay curve described by Eqn. 1.1 would be applicable). Rather the decay was closely described by a stretched exponential function which suggests the presence of a range of different relaxation channels. The long decay times can be connected with the defect levels responsible for the retarded migration and/or the tunnelling recombination of charge carriers, *i.e.* the kinetics is primarily controlled by the excitation rate of impurity ions. Some contribution to the non-exponentiality may also come from the multiple sites for RE^{3+}.

4.3.3. PL excitation spectra

A direct indication of energy transfer can be obtained through the excitation spectra of RE emission. Besides the excitation spectra of intrinsic as well as impurity-related emissions characterize the fundamental absorption edge of the material, the quality of the crystal structure (influenced by growth conditions, implantation, and thermal treatment), and reveal multiphoton relaxation at higher photon energies.

The PL spectra of ZrO_2 and HfO_2 were recorded in the spectral range of 1.5–5.5 eV and the excitation spectra of various emission bands were recorded in the spectral range of 5–20 eV (Fig. 4.9). The graphs (a) and (b) in Fig. 4.9 illustrate the influence of implantation on the emission and excitation spectra. The PL spectrum of an undoped HfO_2 film consists of a strong emission band centered near 4.1 eV and a much weaker emission band at 2.6 eV. The former has been attributed to the recombination of self-trapped excitons [48]. The latter is apparently defect-related. In the PL spectrum of an implanted and intermediately annealed HfO_2 film, the intensity of this emission band has remarkably increased. Another indication of the defective nature of the implanted samples is found in the reduced excitation efficiency of the STE emission when excited with the photon energies exceeding $\sim$7 eV. Such behavior is present even for implanted samples annealed at 1100 °C as shown in Fig. 4.9(c,d). This can be explained as follows. On the excitation near the absorption edge, there is a high probability of the formation of STE states (see *e.g.* [35]), therefore insignificant differences between the PL excitation spectra of implanted and undoped samples can be noticed. At higher excitation energies, however, the photoexcited charge carriers can become free and migrate to the additional defects introduced during the ion implantation process. There they can relax nonradiatively or form a bound excitonic state emitting in a different spectral range.

The emission band located near 4.2 eV has been considered elementary, *i.e.* arising from the recombination of the STE state of a high-quality crystal. We found, however, that the emission in this spectral range was markedly deformed in the case of implanted samples depending on growth temperature of the film, the type of the RE ion implanted, and the post-implantation thermal treatment. The emission generally exhibits several sub-bands suggesting that the emission arises from the recombination of several different types of bound excitons due to the different recombination centers present in the defective crystal. A detailed analysis of the results is, however, beyond the scope of this thesis.

The substantial increase of excitation efficiency at $E \geq 13$ eV could be attributed to the creation of secondary excitations due to the high-energetic charge carriers. Due to this effect, it has been frequently pointed out that ZrO_2 and HfO_2 are promising as X-ray scintillators [48, 80, 148].

Several authors have reported on the observation of the charge transfer absorption band of Eu^{3+} in ZrO_2 located near 250 nm [85, 87, 141]. The present samples did not reveal any excitation band near 250 nm. Most probably this is due to the insufficient quantity of material present in thin films for a direct excitation.

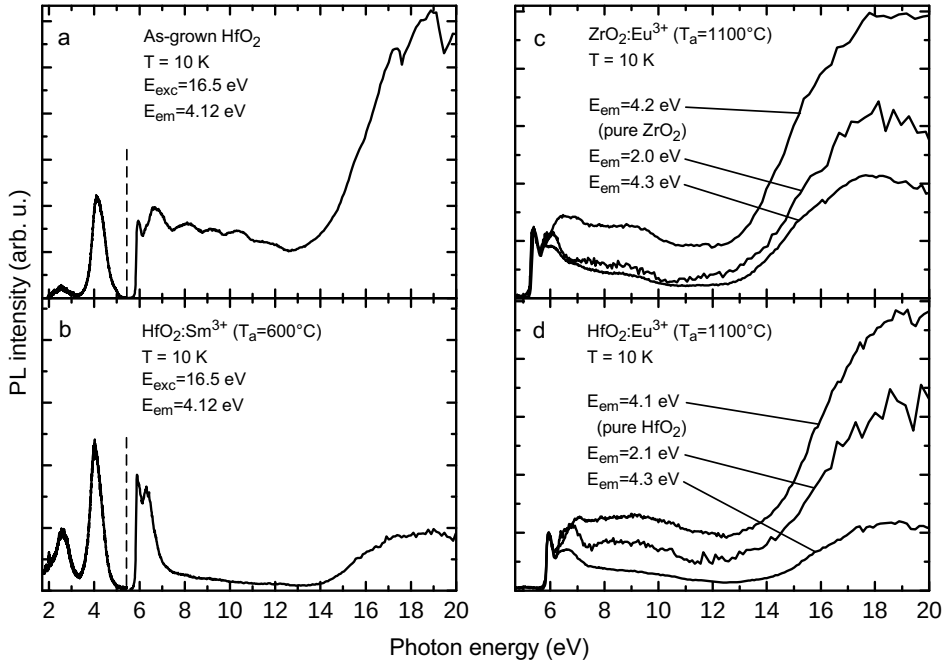

Figure 4.9: Luminescence and its excitation spectra of pure and Eu-doped ZrO_2 and HfO_2 thin films prepared via ALD. The spectra have been measured at 10 K. T_a denotes the annealing temperature. The luminescence spectra were excited at E_{exc}, whereas the excitation spectra were recorded at E_{em}.

4.3.4. Effective cross section of RE excitation

Another, more indirect method for detecting an energy transfer involves measurement of effective cross section of excitation. In order to introduce this quantity we consider first the direct excitation of RE ions. By definition of absorption cross section σ, the time evolution of the concentration of excited RE ions is governed by the following rate equation:

$$\frac{dN^*}{dt} = \sigma\Phi(N - N^*) - \frac{N^*}{\tau}, \tag{4.1}$$

where N denotes the total concentration of optically active RE ions, Φ is the photon flux density, and τ is the decay time of an excited RE ion. The equation applies to the situation where the absorbing state relaxes fast (in comparison to τ) to the emitting state and there is only on type of optical centers present (characterized by a well-defined τ). One can employ the equation and extract the absorption cross section by measuring either the rise time of RE emission or the excitation power dependence of stationary RE emission intensity.

One can extend the equation (4.1) to the situation where the RE impurities are excited via an energy transfer after a band-to-band excitation of the host matrix.

In this case σ has the meaning of an effective cross section of RE excitation. Differently from direct excitation the effective cross section is dependent on the ion concentration. In the case of 100% efficiency of energy transfer one would expect $\sigma = \alpha/N$, where α denotes the absorption coefficient of the material for the excitation beam. For example, in Er^{3+}:Si cross-sections as high as $2 \times 10^{-12}\,cm^2$ has been reported [59].

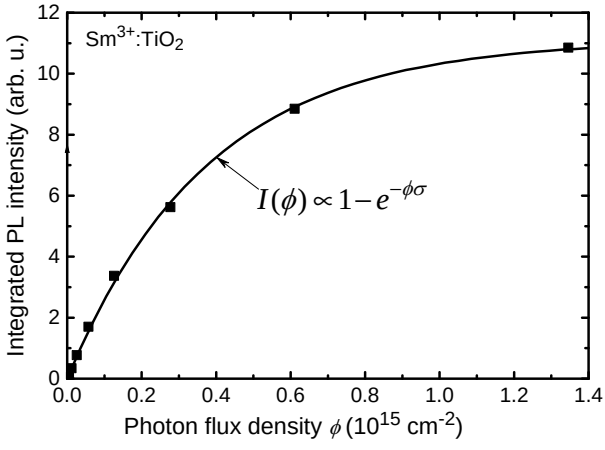

Figure 4.10: Dependence of the TiO_2:Sm^{3+} luminescence intensity on the photon flux density.

In the present case a Nd:YAG pulsed laser operating at 355 nm (3.49 eV) was used for a band-to-band excitation of TiO_2:Sm^{3+}. The pulsed excitation enables more easily achieving saturation of RE emission. As the absorption coefficient of anatase at 3.49 eV is about $4 \times 10^4\,cm^{-1}$ [19], we may assume that the photon flux Φ within the 200 nm film is quite uniform, yet we ignore possible interference effects arising from the multiple reflections at the film surfaces. For a pulse width ($\sim$10 ns) significantly shorter than τ we can ignore the decay term at the right hand side of Eqn. (4.1) during the period of excitation. The remaining equation can be integrated to yield the number of excited ions after the excitation pulse:

$$N^* = N\left(1 - e^{\sigma\phi}\right) \quad \text{with} \quad \phi = \int \Phi(t)\,dt. \tag{4.2}$$

ϕ is the total number of photons per pulse per unit area. The experimentally observed dependence of the luminescence intensity on ϕ along with the best fit to Eqn. (4.2) is depicted in Fig. 4.10. The obtained value of effective cross section is $\sigma = 2.5 \times 10^{-15}\,cm^2$. This significantly exceeds the cross section of direct excitation, which is of the order of $10^{-21}\,cm^2$. Considering that $N = 5 \times 10^{17}\,cm^{-3}$ (by implantation dose) and $\alpha \sim 4 \times 10^4\,cm^{-1}$, the maximum value of σ would be around $8 \times 10^{-14}\,cm^2$, suggesting a quantum efficiency of excitation about 0.03.

The exact physical meaning of σ depends on the details of the energy transfer process. In principle the method could yield more substantial information about the energy transfer process if both RE^{3+} emission as well as any concurrent photoexcitation relaxation channel (*e.g.*, excitonic emission) is simultaneously observed as demonstrated in [73]. In addition, owing to the different effective excitation cross-sections of different emission centers, excitation power dependent changes in the PL spectra can reveal the number of different RE centers involved

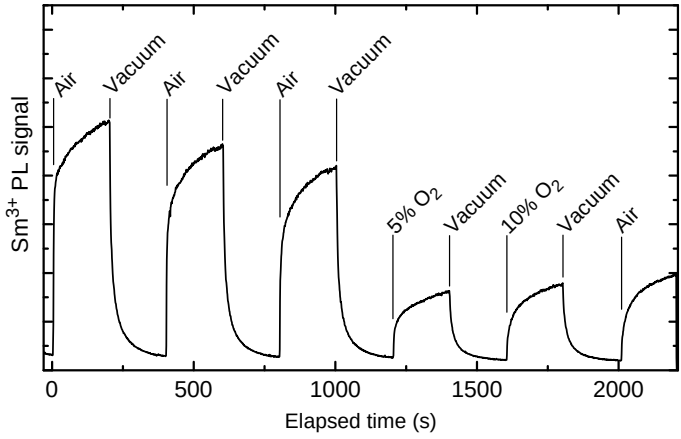

Figure 4.11: Temporal behavior of the Sm^{3+}:TiO_2 nanopowder luminescence intensity in different oxygen-containing ambients.

[149]. In the present case we could not found significant changes in the PL spectra which is in accordance with the time-resolved measurements.

4.3.5. Gas sensing behavior

It is possible that the key to the understanding of the optical processes leading to the excitation of the RE^{3+} ions in the metal-oxides lies in the gas sensing effect that was recently discovered by our research group [150]. It was found that the luminescence signal of Sm^{3+} in TiO_2 is not steady after switching on the excitation but is changing in time, the kinetics and the final saturating intensity depending on the oxygen and water content in the ambient. For the films produced via the ALD method the effect is generally vague. However, the sol-gel-derived films and especially nanopowders exhibit pronounced sensitivity (Fig. 4.11). It is evident that the effect is related to the large surface-to-volume ratio of the porous films and powders. It has been found that *both* the presence of oxygen in ambient gas as well as the UV radiation is required to induce the growth of emission intensity. If the excitation light is blocked the process is stopped. Evacuation of the sample chamber (or replacing O_2 with any other gas) leads to dropping of the signal to a negligible level.

Molecular species adsorbed on the surface of an oxide can inject electrons into or capture them from the conduction band of the material. For example, oxygen molecule exhibits high oxidizing power (high electronegativity) and can acquire one or even two electrons from the conduction band and become a negatively charged chemisorbed entity (most probably O_2^-) [86]. Water molecules in ambient environment, on the other hand, are known to be involved in surface reactions, which results in releasing electrons into the conduction band or holes into the valence band. In the case of a large surface-to-volume ratio the adsorption of oxygen or water can lead to a significant changes in the concentration of conduction

charge carriers. In addition, a space-charge layer (Schottky barrier) is formed on the surface of every crystallite [151]. These effects cause essential changes of material's overall electrical conductivity. Such effects have already enabled using nanocrystalline TiO_2 films in conductivity-based gas- and humidity-sensing devices operating at low temperatures [79, 152]. In our case the basic question is how the trapping or releasing of electrons at the surface is mediated to the luminescence behavior of Sm^{3+} impurities.

A starting point for the interpretation of the gas-sensing effects should be the photoconductivity experiments performed on nanocrystalline TiO_2 [153]. In these measurements, a transient behavior of photoconductivity is observed after switching on the excitation light. The kinetics and final steady-state conductivity depends on the ambient. In air the current achieves its maximum relatively fast whereas in vacuum saturation is achieved in hours. The transient is attributed to the filling of various charge carrier traps especially those due to the adsorbed oxygen species. Such traps are present in large amounts due to the nanoporous nature of the material. At first sight the results of photoconductivity seem to be opposite to our results if the excitation probability of Sm^{3+} is naively connected only to the concentration of photogenerated electron-hole pairs. Our results are also in contrast to other PL measurements where enhancement of PL intensity by H_2O adsorption and quenching of PL emission by O_2 adsorption has been noticed [154]. Therefore some more complicated mechanism must be responsible for the Sm^{3+} activation in these materials.

The supposition that oxygen ambient traps free electrons whereas water injects free electrons seems to suggest that the activation of Sm centers is related to the excess of holes. This assumption, considering the interpretation of photoconductivity, can explain most of the observations. In vacuum there exists no excess of holes as TiO_2 is inherently n-type conductive due to the presence of oxygen vacancies. After exposing the sample to the oxygen, photoexcited electrons begin trapping at the surface. Initially the rate of trapping is fast that explains the initial fast rise of the PL intensity. The experiment shows that the saturating PL intensity is limited by the intensity of excitation.

One could argue about the role of the diffusion of the adsorbed molecular species into the material. However, at room temperature the diffusion of atoms or molecules (other than hydrogen) in the bulk should be considered improbable. According to the experimental data on the oxygen atom diffusion in the metal-oxides [155] the characteristic diffusion length $\sqrt{D\Delta t}$ during the time scale considered is negligible at room temperature. Yet, it might be that in the nanoporous sol-gel materials most of the Sm^{3+} emission is connected to the Sm emission centers located near the surface. In this case the diffusion of ambient molecules into the nanopore network could come into play.

Some gas-sensing effects remain that are not satisfactorily explained by any of the models discussed. For example, it was found that the active state of Sm^{3+} centers is retained if the oxygen is replaced with nitrogen without an intermediate evacuation. Clarification of these peculiarities needs further systematic investigation of samples of different thicknesses and porosities.

Table 6: The ionic radii (due to Shannon [159, 160]) of trivalent RE ions and tetravalent metal ions. CN denotes coordination number.

Ion (CN)	Ionic radius (Å)	Ion (CN)	Ionic radius (Å)
Ti^{4+} (6)	0.61	Sm^{3+} (6)	0.96
Zr^{4+} (7)	0.78	Eu^{3+} (6)	0.95
Hf^{4+} (7)	0.76	Sm^{3+} (7)	1.02
		Eu^{3+} (7)	1.01

4.3.6. Further discussion

When introducing impurities into a crystal, one is, in the first place, interested how the impurity atoms position into the host matrix and form the optical centers. For the RE^{3+}-doped metal(IV)oxides the answer is not trivial because: 1) the RE^{3+} ion do not fit into the Me^{4+} lattice position (Table 6); 2) some local charge compensation is required to replace the tetravalent cation of the host lattice. Presently the best estimate of the lattice position of the trivalent RE ions in these oxides can be drawn from the PL spectra on the symmetry grounds as discussed previously. Full identification of rare earth sites requires generally a combination of luminescence studies with ESR, polarization, and Zeeman techniques. Yet, one can draw parallels to the situation encountered in various titanates doped with either trivalent transition-metal or RE impurities. The crystal structure of the titanates usually contains a similar TiO_6 octahedron that is the basic building block of TiO_2. In the case of Sm^{3+}-doped $BaTiO_3$ it has been found that Sm^{3+} ion can occupy Ti^{4+} as well as Ba^{2+} site [144, 156]. The charge compensation mechanism in Fe^{3+}-doped $SrTiO_3$ has been widely studied by using ESR [157, 158]. It has been confirmed that the Fe^{3+} centers exists where the Fe^{3+} ion is accompanied by a neighboring oxygen vacancy. So in an ideal case we could expect two types of RE^{3+} centers present at equal amounts: a substitutional RE^{3+} ion surrounded by six oxygen atoms and a similar center that forms an aggregate with a neighboring double-ionized oxygen vacancy. Yet, the aggregation of RE^{3+} ion and oxygen vacancy is still disputable due to the large dielectric constant of the host lattices which provides strong screening for the Coulomb attraction between the entities. On the other hand, the large dielectric constant ensures that the centers are stable at room temperature.

Oxygen vacancies are normally present in any oxide material due to an equilibrium between the neutral oxygen molecules in the ambient gas phase and oxygen anions in the lattice. Infrared absorption and photoconductivity measurements have revealed that in TiO_2 (rutile) the oxygen (O^{2-}) vacancy can bound up to two electrons, *i.e.*, it acts as an electron donor. The first and the second ionization (binding) energies have been found to be 0.75 eV and 1.18 eV, respectively [161]. Hence we must admit that there exists several different charge states of the RE^{3+}-bound vacancy, which might influence the energy transfer process as well as the emission properties of the ion.

Understanding of various phenomena, such as charge carrier trapping by im-

purity center, autoionization *etc.* requires knowledge of the level locations of the impurity with respect to the energy bands of the host material. There exist at least two simple routes for estimating the level locations as we can demonstrate in the case of ZrO_2. The first approach is based on the RE charge transfer band that in the case of Eu^{3+}:ZrO_2 is well-known to be located near 250 nm or 5.0 eV. After the charge transfer transition Eu^{2+} is formed. The ground state of Eu^{3+} is about 6 eV below the ground state of Eu^{2+} (Fig. 1.2), consequently it lies about 1 eV below the top of the valence band. The ground state of Sm^{3+}, in turn, is placed about 1 eV above that of Eu^{3+} (Fig. 1.2), *i.e.* it nearly coincides with the top of the valence band. The uncertainty of these estimates is of the order of 0.5 eV. As a second method, we can utilize the fact that Ce^{3+} does not emit in ZrO_2 due to the autoionization of the atom excited to the $5d$ configuration. This is because the $5d$ state is energetically too close to or inside the conduction band. The $4f - 5d$ transition of Ce^{3+} in ZrO_2 is around 2.7 eV and the bandgap of ZrO_2 is around 5.2 eV (Fig. 4.9). Putting the lowest $5d$ state of Ce^{3+} at 5.2 eV, the ground state is 2.5 eV above the valence band edge. The ground state of Eu^{3+} is 4.1 eV lower which places it about 1.6 eV below the top of the valence band. This is, however, the lower limit, because the $5d$ state of Ce^{3+} can be well inside the conduction band. Therefore the result is in accordance with the previous estimate. It is evident that the ground state level of divalent Eu and Sm is located at or above the bottom of the conduction band which allows delocalization of the electron and makes existence of divalent charge state of these ions improbable in the matrices.

We believe that the exact route of the energy transfer from host to guest taking place in the RE-doped metal-oxides cannot be identified based on the presented results of PL-measurements. As an increase in temperature leads to an increase of the Sm^{3+} emission in anatase, but also to a decrease of the trapped excitonic emission intensity (Fig. 4.6), an energy transfer (radiative or nonradiative) from these excitonic states cannot be responsible for Sm^{3+} excitation (in which case a common dependence on temperature would be expected). Similarly, hot electron impact seems to be irrelevant in the photoexcitation of the materials, at least for the excitation photon energies close to the band-gap value. In ZrO_2 and HfO_2 the energy migrates to RE ions most probably in the form of free excitons as also supported by the observation of excitonic peaks in the RE excitation spectra (Fig. 4.9). However, in TiO_2 of anatase phase the self-trapping of excitons is favored. In this matrix a sequential trapping of an electron and a hole by the impurity center probably takes place. These processes are followed by an Auger-type energy transfer during the recombination of the impurity-bound electron-hole pair. This is the most frequently encountered scenario in various semiconductor systems [59, 72, 73]. Furthermore, it has been suggested that this type of energy transfer should be applicable to other RE-doped solids as well. However, for a direct evidence of this model more complicated measurements are needed (*e.g.* two-color spectroscopy [72]).

4.4. Conclusion

The present work has confirmed that Sm^{3+}- and Eu^{3+}-activated TiO_2, ZrO_2, and HfO_2 can be prepared by implanting ALD-grown films as well as via sol-gel route and the materials are promising for luminescence applications. It was found that the emission can be excited via a band-to-band excitation of the host materials indicating an energy transfer from host to guest, Emission efficiency of the materials can be significantly increased by a proper thermal treatment. With respect to emission intensity the most promising system seems to be Eu^{3+}:HfO_2. The well-resolved fine structure as well as similar decay rate of all spectral lines indicate that the ions are fit into regular positions in all matrices studied. Unfortunately, the two routes of preparation result in different thickness and microstructure of the samples, which prevents a quantitative comparison of the luminescence properties of differently prepared samples.

A number of developments are still possible in this direction. Of fundamental interest is the energy transfer mechanism that still remains unidentified. A thorough understanding of the energy transfer mechanism could enable predicting more promising combinations of host and guest. The detailed study of both the self-trapped as well as any defect-related excitonic emissions and their temperature dependencies could reveal their connection to the energy transfer process. RE excitation spectra within the sub-bandgap energy range could reveal defect levels that are involved in the energy transfer. From the applicational point of view the determination of optimum concentrations of RE ions and, in some cases, higher annealing treatments are required. The ion implantation incorporates the RE ions at trace concentrations that is suitable for fundamental investigation but does not enable considering practical applications as phosphors, laser media, *etc.* The quantities involved in sol-gel process are also below the limits where the cross-relaxation-induced quenching becomes significant. It might be the case that the ion implantation as a destructive method is not suitable for introducing massive amounts of impurities into a crystalline material. In that case other possibilities for incorporating impurities into ALD-grown films must be considered.

SUMMARY

OPTICAL INVESTIGATION OF METAL-OXIDE THIN FILMS

This PhD thesis comprises the results of a spectroscopic study of pure and RE-doped thin films of TiO_2, ZrO_2, and HfO_2. Europium and samarium have been used as optical activators. These optical materials have remarkable application potential as phosphors, in optical gas sensing, as waveguides *etc.* Two preparation routes have been employed for obtaining the materials: atomic layer deposition (ALD) and sol-gel technique. ALD films have been doped by using ion implantation. In addition to nanothin films, sol-gel method allows preparation of nanosized powders as well.

The original contribution has been divided into two parts.

Chapter 3 describes the study of the waveguiding properties of atomic layer deposited thin films of pure and Sm-doped TiO_2. It was found that the waveguiding structure of the films strongly influences the spectral-directional characteristics of the photoluminescence (PL). When viewed at the nearly in-plane direction, the broadband PL spectrum was modified into relatively sharp linearly polarized spectral resonances attributed to the leaky modes of the waveguide close to the total internal reflection. The observed peculiarities were explained within classical as well as quantum electrodynamic treatment. The results indicate that the ALD method has potential for preparation of waveguiding layers of the metal oxides though some obstacles remain to overcome. Also, the effect of spectral narrowing is proposed as a way to characterize thin films exhibiting broad luminescence bands.

Chapter 4 describes the results of developing rare-earth-doped metal-oxide luminescent materials. The main results and conclusions are as follows:

- The ion implantation of the oxides with samarium and europium leads to the formation of Sm^{3+} and Eu^{3+} emitting centers after a proper annealing treatment. Combined RE luminescence efficiency and decay kinetics measurements of ion-implanted samples were used for determination of optimal annealing conditions.
- It was established that the trivalent ions can be excited indirectly via optical band-to-band excitation of the host matrix. The effective cross section of Sm^{3+} excitation in TiO_2 at 355 nm was determined as $2.5 \times 10^{-15}\,cm^2$. The estimated quantum efficiency of excitation was $\sim$0.03.
- The optimum annealing temperature for Sm^{3+}:TiO_2 was $\sim$700 °C. The rapid quenching of PL at higher-temperature annealing treatments was attributed either to the phase transition from anatase to rutile polymorph or agglomeration of impurities due to an increased diffusion rate.
- It was found that RE doping modifies the PL spectrum related to the trapped excitonic states. The decay kinetics of the excitonic emission follows asymptotically a power law (as in a pure anatase) that is characteristic to a tunnelling recombination of randomly distributed electrons and holes.

- It was possible to use Eu^{3+} as an optical probe of local environment. From the splitting of ${}^5D_0 \rightarrow {}^7F_0$ transition it is concluded that at least two different optical centers exist in RE-doped ZrO_2 and HfO_2. From the ratio of ${}^5D_0 \rightarrow {}^7F_2$ and ${}^5D_0 \rightarrow {}^7F_1$ transitions the establishment of a monoclinic surrounding for Eu^{3+} is observed as the annealing temperature is increased.
- It was found that Sm^{3+} emission in nanoporous TiO_2 materials is sensitive to the ambient gaseous environment suggesting application potential in optical gas sensing.

SUMMARY IN ESTONIAN

ÕHUKESTE METALLOKSIIDKILEDE OPTILISED UURINGUD

Käesolev väitekiri koondab puhaste ja legeeritud TiO_2, ZrO_2 ning HfO_2 nanomaterjalide spektroskoopiliste uuringute tulemused. Optiliste lisanditena on kasutatud euroopiumi ning samaariumi. Saadud optilised materjalid omavad rakenduspotentsiaali luminofooridena, optilises gaasisensoorikas, lainejuhtidena jm. Materjalide prepareerimiseks on kasutatud kahte erinevat meetodit: aatomikihtsadestamist ning sool-geel meetodit. Aatomkihtsadestatud kilede legeerimiseks rakendati ioonimplantatsiooni. Sool-geel meetod võimaldas valmistada ka nanomõõdus pulbrilisi materjale.

Originaalse uurimistöö kirjeldus ning tulemused on jaotatud kahte ossa.

Peatükk 3 kirjeldab aatomkihtsadestatud õhukeste TiO_2 kilede lainejuhtomaduste uuringuid. Täheldati, et nende kilede lainejuhtstruktuur mõjutab tugevasti kile luminestsentsi spektraalseid ja suunakarakteristikuid. Laiaribalises kiirguses, mida vaadeldi väikese nurga all kaldu kile pinna suhtes, ilmnesid suhteliselt kitsad lineaarselt polariseeritud spektraalsed resonantsid mille tekke võib omistada lainejuhi lekkemoodidele täieliku sisepeegelduse lähedal. Jälgitud efektid seletati nii klassikalise kui ka kvantelektrodünaamika käsitluses. Tulemused näitavad, et aatomkihtsadestamine on perspektiivne meetod lainejuhtstruktuuride valmistamiseks.

Peatükk 4 annab ülevaate haruldaste muldmetallidega legeeritud metalloksiidide kui uudsete luminestsentsmaterjalide optiliste omaduste uuringust. Põhilised tulemused ja järeldused on järgmised:

- Samaariumi ja euroopimiga ioonimplanteeritud oksiidkiledes moodustusid Sm^{3+} ja Eu^{3+} kiirgustsentrid peale sobilikku lõõmutustöötlust. Luminestsentsi efektiivsuse ja kineetika põhjal määrati optimaalsed lõõmutustingimused.
- Selgus, et lisandioone on võimalik ergastada kaudselt põhiaine tsoon-tsoon ergastamise kaudu. Sm^{3+}:TiO_2 ergstamise efektiivseks ristlõikeks lainepikkusel 355 nm määrati $2.5 \times 10^{-15}\,\mathrm{cm}^2$. Ergastamise kvantsaagiseks hinnati 0.03.
- Optimaalseks lõõmutustemperatuuriks Sm^{3+}:TiO_2 jaoks osutus $\sim$700 °C. Järeldati, et luminestsentsi pärssimist kõrgematel lõõmutustemperatuuridel tingib kas põhiaine faasi muutus anataasist rutiiliks või lisandite difusioonist tingitud aglomeratsioon.
- Täheldati, et legeerimine põhjustab märgatavaid muutusi lõksustunud eksitonide kiirgusriba kujus. Eksitonkiirguse kustumiskineetika järgis asümptootiliselt astmeseadust, mis on iseloomulik tunnelrekombinatsioonile juhuslikult paigutunud elektronide ja aukude vahel.
- Eu^{3+} ioone kasutati optilise struktuuri-indikaatorina. Ülemineku $^5D_0 \rightarrow {}^7F_0$ lõhenemisest järeldati vähemalt kahe erineva optilise tsentri olemasolu dopeeritud ZrO_2 ja HfO_2 maatriksites. Üleminekute $^5D_0 \rightarrow {}^7F_2$ ja $^5D_0 \rightarrow {}^7F_1$

intensiivsuste suhte kaudu jälgiti monokliinse faasi moodustumist ZrO_2-s ja HfO_2-s lõõmutustemperatuuri tõstmisel.

- Leiti, et Sm^{3+} luminestsentsi intensiivsus nanopoorsetes TiO_2 materjalides on tundlik ümbritseva gaasikeskkonna suhtes, mis annab nimetatud materjalile uudse rakenduse optilises gaasisensoorikas.

ACKNOWLEDGEMENTS

The work described in this thesis has been carried out mainly in the Institute of Physics, University of Tartu in the years 2002–2006. Several people from this institute and beyond have contributed, directly or indirectly, to the research.

First of all I would like to express my gratitude to my supervisor dr. Ilmo Sildos for his guidance and support. I'm also grateful to dr. Olev Sild for fruitful discussions on theoretical subjects. Dr. Marco Kirm is kindly acknowledged for his help in synchrotron radiation measurements and for sharing his knowledge on rare earths and wide-gap materials.

Several people must be acknowledged in connection to the sample preparation. First of all, I'm owing gratitude to Jaan Aarik who have provided us the atomic-layer-deposited samples. I acknowledge also Tanel Tätte and Valter Reedo for their labor in sol-gel preparation. The author is grateful to Prof. A. Winnacker from Erlangen University for the possibility of implanting samples. Uppsala University if acknowledged for the possibility to use the ion-implantation facility and spectroscopic ellipsometer via the program "Access to Research Infrastructure action of the Improving Human Potential Programme" of European Community.

And last, but not least, I appreciate the support of the colleagues from the Laboratory of Laser Spectroscopy of the Institute of Physics, especially Sven Lange, Argo Lukner, and Martti Pärs, whose help in carrying out experiments and useful discussions contributed much to the success of the research.

The work was supported during these years by the Estonian Science Foundation (Grants Nos. 4512, 5864, and 5861).

REFERENCES

[1] S. Shionoya and W. M. Yen (eds.), *Phosphor Handbook* (CRC, Boca Raton, 1999).

[2] C. R. Ronda, J. Alloys Comp. **225**, 534–538 (1995).

[3] I. Bergman, Nature **218**, 396 (1968).

[4] O. S. Wolfbeis, in: *Biomedical Optical Instrumentation and Laser-Assisted Biotechnology*, edited by A. M. Verga-Scheggi (Kluwer Academic Publishers, 1996), pp. 327–337.

[5] R. Moncorgé, L. D. Merkle, and B. Zandi, MRS Bulletin **24**, 21–27 (1999).

[6] C. R. Ronda, T. Jüstel, and H. Nikol, J. Alloys and Compounds **275-277**, 669–676 (1998).

[7] J. Ballato, J. Lewis, and P. Holloway, MRS Bulletin **24**, 51–56 (1999).

[8] A. J. Wojtowicz, Nucl. Instr. Meth. Phys. Res. A **486**, 201–207 (2002).

[9] R. T. Wegh, H. Donker, K. D. Oskam, and A. Meijerink, Science **283**, 663–666 (1999).

[10] C. Lushchik, E. Feldbach, A. Frorip, M. Kirm, A. Lushchik, A. Maaroos, and I. Martinson, Phys. Rev. B **60**, 502–510 (1999).

[11] V. Petkov, G. Holzhüter, U. Tröge, T. Gerber, and B. Himmel, J. Non-cryst. Solids **231**, 17–30 (1998).

[12] A. Fujishima and K. Honda, Nature **238**, 37–38 (1972).

[13] A. Fujishima, T. N. Rao, and D. A. Tryk, J. Photochem. Photobiol. C **1**, 1–12 (2000).

[14] R. Wang, K. Hashimoto, and A. Fujishima, Nature **388**, 431–432 (1997).

[15] B. O'Regan and M. Grätzel, Nature **353**, 737–739 (1991).

[16] H. Tang, F. Lévy, H. Berger, and P. E. Schmid, Phys. Rev. B **52**, 7771–7774 (1995).

[17] M. W. Ribarsky, in: *Handbook of Optical Constants*, edited by E. Palik (Academic Press, Orlando, 1985), pp. 795–804.

[18] G. Hass, Vacuum **2**, 331–345 (1952).

[19] H. Tang, K. Prasad, R. Sanjinès, P. E. Schmid, and F. Lévy, J. Appl. Phys. **75**, 2042–2046 (1994).

[20] S. Roberts, Phys. Rev. **76**, 1215–1220 (1949).

[21] C. J. Howard, R. J. Hill, and B. E. Reichert, Acta Crystallogr. **B44**, 116–120 (1988).

[22] J. Adam and M. D. Rogers, IEEE J. Quant. Electr. **12**, 951–956 (1959).

[23] J. Wang, H. P. Li, and R. Stevens, J. Mater. Sci. **27**, 5397–5430 (1992).

[24] N. M. Balzaretti and J. A. H. da Jornada, Phys. Rev. B **52**, 9266–9269

(1995).

[25] R. H. French, S. J. Glass, F. S. Ohuchi, Y.-N. Xu, and W. Y. Ching, Phys. Rev. B **49**, 5133–5142 (1994).

[26] D. L. Wood and K. Nassau, Appl. Optics **21**, 2978–2981 (1982).

[27] C. R. Aita and C.-K. Kwok, J. Am. Ceram. Soc. **73**, 3209–3214 (1990).

[28] C. R. Aita, E. E. Hoppe, and R. S. Sorbello, Appl. Phys. Lett. **82**, 677–679 (2003).

[29] M. Balog, M. Schieber, M. Michman, and S. Patai, Thin Solid Films **41**, 247–259 (1977).

[30] D. Vanderbilt, X. Zhao, and D. Ceresoli, Thin Solid Films **486**, 125–128 (2005).

[31] L. G. J. de Haart and G. Blasse, J. Solid State Chem. **61**, 135–136 (1986).

[32] H. Tang, H. Berger, P. E. Schmid, and F. Lévy, Solid State Comm. **87**, 847–850 (1993).

[33] H. Tang, H. Berger, P. E. Schmid, and F. Lévy, Solid State Comm. **92**, 267–271 (1994).

[34] A. Suisalu, J. Aarik, H. Mändar, and I. Sildos, Thin Solid Films **336**, 295–298 (1998).

[35] M. Watanabe, T. Hayashi, H. Yagasaki, and S. Sasaki, Intern. J. Mod. Phys. B **15**, 3997–4000 (2001).

[36] M. Watanabe and T. Hayashi, J. Lumin. **112**, 88–91 (2005).

[37] D. G. Thomas, J. J. Hopfield, and W. M. Augustyniak, Phys. Rev. **140**, A202–A220 (1965).

[38] C. J. Delberg, D. L. Dexter, and P. H. Yuster, Phys. Rev. B **17**, 4765–4774 (1978).

[39] I. Sildos, A. Suisalu, J. Aarik, T. Sekiya, and S. Kurita, J. Lumin. **87-89**, 290–292 (2000).

[40] K. S. Song and R. T. Williams, *Self-trapped Excitons* (Springer-Verlag, 1993).

[41] I. Sildos, A. Suisalu, V. Kiisk, M. Schuisky, H. Mändar, T. Uustare, and J. Aarik, Proc. SPIE **4086**, 427–430 (2000).

[42] S. Block, J. A. H. da Jornada, and G. J. Piermarini, J. Am. Ceram. Soc. **68**, 497–499 (1985).

[43] A. S. Foster, F. L. Gejo, A. L. Shluger, and R. M. Nieminen, Phys. Rev. B **65**, 174117 (2002).

[44] E. V. Stefanovich and A. L. Scluger, Phys. Rev. B **49**, 11560–11571 (1994).

[45] S. Shukla, S. Seal, R. Vij, S. Bandyopadhyay, and Z. Rahman, Nano Letters **2**, 989–993 (2002).

[46] J. E. Jaffe, R. A. Bachorz, and M. Gutowski, Phys. Rev. B **72**, 114107 (2005).

[47] J. Aarik, H. Mändar, M. Kirm, and L. Pung, Thin Solid Films **466**, 41–47 (2004).

[48] M. Kirm, J. Aarik, M. Jürgens, and I. Sildos, Nucl. Instr. Meth. Phys. Res. A **537**, 251–255 (2005).

[49] N. G. Petrik, D. P. Taylor, and T. M. Orlando, J. Appl. Phys. **85**, 6770–6776 (1999).

[50] R. Asahi, Y. Taga, W. Mannstadt, and A. J. Freeman, Phys. Rev. B **61**, 7459–7465 (2000).

[51] A. S. Foster, V. B. Sulimov, F. L. Gejo, A. L. Shluger, and R. M. Nieminen, Phys. Rev. B **64**, 224108 (2001).

[52] S. Weissmantel, G. Reisse, B. Keiper, U. Broulik, H. Johansen, and R. Scholz, Appl. Surf. Sci. **108**, 1–7 (1997).

[53] M. Alvisia, M. D. Giulioa, S. G. Marroneb, M. R. Perronec, M. L. Protopapac, A. Valentinib, and L. Vasanelli, Thin Solid Films **358**, 250–258 (2000).

[54] D. Grosso and P. A. Sermon, Thin Solid Films **368**, 116–124 (2000).

[55] G. D. Wilk, R. M. Wallace, and J. M. Anthony, J. Appl. Phys. **89**, 5243–5275 (2001).

[56] B. G. Wybourne, *Spectroscopic properties of rare earths* (Wiley, New York, 1965).

[57] G. H. Dieke, *Spectra and energy levels of rare earth ions in crystals* (Interscience Publishers, New York, 1968).

[58] R. W. Equall, Y. Sun, and L. Cone, Phys. Rev. Lett. **72**, 2179–2182 (1994).

[59] A. J. Kenyon, Progr. Quantum Electronics **26**, 225–284 (2002).

[60] T. Kano, in: *Phosphor Handbook*, edited by S. Shionoya and W. M. Yen (CRC Press, Boca Raton, 1999), pp. 177–200.

[61] P. Dorenbos, J. Phys. Cond. Matt. **15**, 8417–8434 (2003).

[62] P. Dorenbos, J. Phys. Cond. Matt. **15**, 575–594 (2003).

[63] M. D. Shinn, W. A. Sibley, M. G. Drexhage, and R. N. Brown, Phys. Rev. B **27**, 6635–6648 (1983).

[64] T. Ohsaka, F. Izumi, and Y. Fujiki, J. Raman Spectrosc. **7**, 321–3240 (1978).

[65] P. E. Quintard, P. Barbéris, A. P. Mirgorodsky, and T. Merle-Méjean, J. Am. Ceram. Soc. **85**, 1745–1749 (2002).

[66] A. Jayaraman, S. Y. Wang, S. K. Sharma, and L. C. Ming, Phys. Rev. B **48**, 9205–9211 (1993).

[67] M. Inokuti and F. Hirayama, J. Chem. Phys. **43**, 1978–1989 (1965).

[68] M. N. Berberan-Santos, E. N. Bodunov, and B. Valeur, Chem. Phys. **315**, 171–182 (2005).

[69] A. N. Belsky and J. C. Krupa, Displays **19**, 185–196 (1999).

[70] D. L. Dexter, J. Chem. Phys. **21**, 836–850 (1953).

[71] C. Buchal, S. Wang, F. Lu, R. Carius, and S. Coffa, Nucl. Instr. Meth. Phys. Res. B **190**, 40–46 (2002).

[72] M. A. J. Klik, T. Gregorkiewicz, I. V. Bradley, and J.-P. R. Wells, Phys. Rev. Lett. **89**, 227401 (2002).

[73] O. Gusev, M. Bresler, P. E. Pak, I. N. Yassievich, M. Forcales, N. Q. Vinh, and T. Gregorkiewicz, Phys. Rev. B **64**, 075302 (2001).

[74] M. Balog, M. Schieber, M. Michman, and S. Patai, Thin Solid Films **47**, 109–120 (1977).

[75] C. Urlacher, C. M. de Lucas, E. Bernstein, B. Jacquier, and J. Mugnier, Optical Materials **12**, 19 (1999).

[76] R. Reisfeld, M. Zelner, and A. Patra, J. Alloys Comp. **300**, 147–151 (2000).

[77] A. Conde-Gallardo, M. Garcia-Rocha, R. Palomino-Merino, M. P. Velásquez-Quesada, and I. Hernández-Calderón, Appl. Surf. Sci. **212-213**, 583–588 (2003).

[78] R. R. G. calves, G. Carturan, L. Zampedri, M. Ferrari, M. Montagna, A. Chiasera, G. C. Righini, S. Pelli, S. J. L. Ribeiro, and Y. Messaddeq, Appl. Phys. Lett. **81**, 28–30 (2002).

[79] W.-P. Tai and J.-E. Oh, Thin Solid Films **422**, 220–224 (2002).

[80] M. V.-I. n ez, C. L. Luyer, C. Dujardin, and J. Mugnier, Mat. Sci. Eng. B **105**, 12–15 (2003).

[81] K. L. Frindell, M. H. Bartl, M. R. Robinson, G. C. Bazan, A. Popitsch, and G. D. Stucky, J. Solid State Chem. **172**, 81–88 (2003).

[82] E. D. la Rosa-Cruz, L. A. Diaz-Torres, P. Salas, R. A. Rodriguez, and G. A. Kumar, J. Appl. Phys. **94**, 3509–3515 (2003).

[83] B. H. Lee, L. Kang, R. Nieh, W. Qi, and J. C. Lee, Appl. Phys. Lett. **76**, 1926–1928 (2000).

[84] P. Zeman and S. Takabayashi, J. Vac. Sci. Tech. A **20**, 388–393 (2002).

[85] K. Kuratani, M. Mizuhata, A. Kajinami, and S. Deki, J. Alloys Comp. **408-412**, 711–716 (2006).

[86] N. Golego, S. A. Studenikin, and M. Cocivera, Phys. Rev. B **61**, 8262–8269 (2000).

[87] Z. W. Quan, L. S. Wang, and J. Lin, Mat. Res. Bull. **40**, 810–820 (2005).

[88] M. Ritala and M. Leskela, in: *Handbook of Thin Film Materials*, edited by H. S. Nalwa (Academic Press, 2002), vol. 1.

[89] J. Aarik, A. Aidla, A.-A. Kiisler, T. Uustare, and V. Sammelselg, Thin Solid Films **340**, 110–116 (1999).

[90] J. Aarik, A. Aidla, H. Mändar, and T. Uustare, Appl. Surf. Sci. **172**, 148–158 (2001).

[91] A. Rosental, P. Adamson, A. Gerst, and A. Niilisk, Appl. Surf. Sci. **107**, 178–183 (1996).

[92] A. Rosental, A. Tarre, P. Adamson, A. Gerst, A. Kasikov, and A. Niilisk, Appl. Surf. Sci. **142**, 204–209 (1999).

[93] M. Ritala, M. Leskelä, E. Nykänen, P. Soininen, and L. Niinistö, Thin Solid Films **225**, 288–295 (1993).

[94] J. Aarik, A. Aidla, H. Mändar, T. Uustare, M. Schuisky, and A. Hårsta, J. Cryst. Growth **242**, 189–198 (2002).

[95] A. Rahtu and M. Ritala, Chemical Vapor Deposition **8**, 21–28 (2002).

[96] J. P. Lee, H. K. Kim, C. R. Park, G. Park, H. T. Kwak, S. M. Koo, and M. Sung, J. Phys. Chem. B **107**, 8997–9002 (2003).

[97] M. Schuisky, K. Kukli, J. Aarik, J. Lu, and A. Hårsta, J. Cryst. Growth **235**, 293–299 (2002).

[98] J. Aarik, A. Aidla, H. Mändar, V. Sammelselg, and T. Uustare, J. Cryst. Growth **220**, 105–113 (2000).

[99] J. Aarik, A. Aidla, H. Mändar, T. Uustare, and V. Sammelselg, Thin Solid Films **408**, 97–103 (2002).

[100] J. Aarik, J. Sundqvist, A. Aidla, J. Lu, T. Sajavaara, K. Kukli, and A. Hårsta, Thin Solid Films **418**, 69–72 (2002).

[101] O. Sneh, R. B. Clark-Phelps, A. R. Londergan, J. Winkler, and T. E. Seidel, Thin Solid Films **402**, 248–261 (2002).

[102] C. J. Brinker and G. W. Scherer (eds.), *Sol-gel science: The physics and chemistry of sol-gel processing* (Academic Press, New York, 1990).

[103] I. Sildos, S. Lange, T. Tätte, V. Kiisk, M. Kirm, and J. Aarik, MRS Proceedings **796**, 70 (2004).

[104] V. Jacobsen, T. Tätte, R. Branscheid, U. Mäeorg, K. Saal, I. Kink, A. Lõhmus, and M. Kreiter, Ultramicroscopy **104**, 39–45 (2005).

[105] L. D. Landau and V. G. Levich, Acta Physicochim. URSS **17**, 42 (1942).

[106] D. Meyerhofer, J. Appl. Phys. **49**, 3993–3997 (1978).

[107] P. D. Townsend, P. J. Chandler, and L. Zhang, *Optical Effects of Ion Implantation* (Cambridge University Press, Cambridge, 1994).

[108] M. S. Janson, M. K. Linnarsson, A. Hallén, and B. G. Svensson, J. Appl. Phys. **93**, 8903–8909 (2003).

[109] K. Suzuki and Y. Morisaki, IEEE Trans. Electron Devices **ED-49**, 1836–1838 (2002).

[110] J. Asher, Nucl. Instr. Meth. Phys. Res. B **89**, 315–321 (1994).

[111] C. Kittel, *Introduction to Solid State Physics* (Wiley, New York, 1996), 7th edn.

[112] T. Sekiya, K. Ichimura, M. Igarashi, and S. Kurita, J. Phys. Chem. Solids

61, 1237–1242 (2000).

[113] F. Lu, A. Rizzi, R. Carius, and C. H. Lei, J. Phys. D **37**, 1544–1547 (2004).

[114] A. Polman, J. Appl. Phys. **82**, 1–39 (1997).

[115] J. F. Ziegler, J. P. Biersack, and U. Littmark, *The Stopping and Range of Ions in Solids* (Pergamon Press, New York, 1985).

[116] *Web site of SRIM software*, `http://www.srim.org`.

[117] D. Kleppner, Phys. Rev. Lett. **47**, 233–236 (1981).

[118] F. Goy, J. M. Raimond, M. Gross, and S. Haroche, Phys. Rev. Lett. **50**, 1903–1906 (1983).

[119] E. Burstein and C. Weisbuch (eds.), *Confined Electrons and Photons* (Plenum Press, New York, 1995).

[120] H. Benisty, J.-M. Gérard, R. Houdré, J. Rarity, and C. Weisbuch (eds.), *Confined Photon Systems: Fundamentals and Applications* (Springer, Berlin, 1999).

[121] A. Serpengüzel, A. Aydinli, and A. Bek, J. Non-cryst. Solids **227**, 1142–1145 (1998).

[122] I. Abram, I. Robert, and R. Kuszelewicz, IEEE J. Quant. Electr. **34**, 71–76 (1998).

[123] D. T. Schaafsma and D. H.Christensen, Phys. Rev. B **54**, 14618–14622 (1996).

[124] J. L. Shen, J. Y. Chang, H. C. Liu, W. C. Chou, Y. F. Chen, T. Jung, and M. C. Wu, Solid State Comm. **116**, 431–435 (2000).

[125] V. Kiisk, I. Sildos, A. Suisalu, and J. Aarik, Thin Solid Films **4000**, 130–133 (2001).

[126] J. Valenta, T. Ostatnický, I. Pelant, R. G. Elliman, J. Linnros, and B. Hönerlage, J. Appl. Phys. **96**, 5222–5225 (2004).

[127] A. Penzkofer, W. Holzer, H. Tillmann, and H. Hörhold, Optics Comm. **229**, 279–290 (2004).

[128] T. Ostatnický, J. Valenta, I. Pelant, K. Luterová, R. G. Elliman, S. Cheylan, and B. Hönerlage, Optical Materials **27**, 781–786 (2005).

[129] K. Luterová, M. Cazzanelli, J.-P. Likforman, D. Navarro, J. Valenta, T. Ostatnický, K. Dohnalova, S. Cheylan, P. Gilliot, B. Hönerlage, L. Pavesi, and I. Pelant, Optical Materials **27**, 750–755 (2005).

[130] R. Baets, P. Bienstman, and R. Bockstaele, in: *Confined Photon Systems: Fundamentals and Applications*, edited by H. Benisty, J.-M. Gérard, R. Houdré, J. Rarity, and C. Weisbuch (Springer, Berlin, 1999), pp. 38–79.

[131] R. C. Smith, M. Tiezhong, N. Hoilien, L. Y. Tsung, M. J. Bevan, L. Colombo, J. Roberts, S. A. Campbell, and W. L. Gladfelter, Adv. Mater. Opt. Electron. **10**, 105–114 (2000).

[132] D. R. G. Mitchell, G. Triani, D. J. Attard, K. S. Finnie, P. J. Evans, C. J. Barbé, and J. R. Bartlett, Smart Mater. Struct. **15**, S57–S64 (2006).

[133] J. Aarik, A. Aidla, T. Uustare, and V. Sammelselg, Thin Solid Films **148**, 268–275 (1995).

[134] A. Kasikov, J. Aarik, H. Mändar, M. Moppel, M. Pärs, and T. Uustare, J. Phys. D **39**, 54–60 (2006).

[135] J. D. Jackson, *Classical Electrodynamics* (Wiley, New York, 1999), 3rd edn.

[136] E. Hecht, *Optics* (Addison-Wesley, New York, 1987), 2nd edn.

[137] D. Marcuse, *Theory of dielectric optical waveguides* (Academic Press, London, 1987), 2nd edn.

[138] T. Sekiya, M. Tasaki, K. Wakabayashi, and S. Kurita, J. Lumin. **108**, 69–73 (2004).

[139] E. D. la Rosa-Cruz, L. A. Diaz-Torres, P. Salas, D. Mendoza, J. M. Hernandez, and V. M. Castano, Optical Materials **19**, 195–199 (2002).

[140] Z. Assefa, R. G. Haire, and P. E. Raison, Spectrochim. Acta A **60**, 89–95 (2004).

[141] L. Chen, Y. Liu, and Y. Li, J. Alloys Comp. **381**, 266–271 (2004).

[142] R. Wang, K. Hashimoto, and A. Fujishima, Optical Materials **28**, 1222–1226 (2006).

[143] B. A. Wilson, W. M. Yen, J. Hegarty, and G. F. Imbusch, Phys. Rev. B **19**, 4238–4250 (1979).

[144] S. Makishima, K. Hasegawa, and S. Shionoya, J. Phys. Soc. Jpn. **20**, 2147–2151 (1965).

[145] J.-G. Li, X. Wang, K. Watanabe, and T. Ishigaki, J. Phys. Chem. B **110**, 1121–1127 (2006).

[146] M. Gaft, G. Panczer, R. Reisfeld, I. Shinno, B. Champagnon, and G. Boulon, J. Lumin. **87-89**, 1032–1035 (2000).

[147] A. Braud, J. L. Doualan, R. Moncorge, B. Pipeleers, and A. Vantomme, Mat. Sci. Eng. B **105**, 101–105 (2003).

[148] N. V. Guerassimova, I. A. Kamenskikh, V. V. Mikhailin, I. N. Shpinkov, D. A. Spassky, E. E. Lomonova, M. A. Borik, N. I. Markov, V. A. Panov, M. A. Vishnjakova, M. Kirm, and G. Zimmerer, Nucl. Instr. Meth. Phys. Res. A **486**, 234–238 (2002).

[149] L. Bodiou, A. Oussif, A. Braud, J.-L. Doulan, R. Moncorgé, K. Lorenz, and E. Alves, Opt. Mat. **28**, 780–784 (2006).

[150] V. Reedo, S. Lange, V. Kiisk, A. Lukner, T. Tätte, and I. Sildos, Proc. SPIE **5946**, 59460F (2005).

[151] V. Lantto, T. T. Rantala, and T. S. Rantala, J. Eur. Cer. Soc. **21**, 1961–1965 (2001).

[152] W. Gopel and K. D. Schierbaum, Sensors and Actuators B **26-27**, 1–12 (1995).

[153] J. Nelson, A. M. Eppler, and I. M. Ballard, J. Photochem. Photobiol. A **148**, 25–31 (2002).

[154] A. L. Linsebigler, G. Lu, and J. T. Yates, Chem. Rev. **95**, 735–758 (1995).

[155] U. Brossmann and R. Würschum, J. Appl. Phys. **85**, 7646–7654 (1999).

[156] S. Makishima, K. Hasegawa, and S. Shionoya, J. Phys. Chem. Solids **23**, 749–757 (1962).

[157] E. S. Kirkpatrick, K. A. Müller, and R. S. Rubin, Phys. Rev. **135**, A86–A90 (1964).

[158] R. L. Berney and D. L. Cowan, Phys. Rev. B **23**, 37–50 (1981).

[159] R. D. Shannon, Acta Crystallogr. **A32**, 751–767 (1976).

[160] D. R. Lide (ed.), *CRC Handbook of Chemistry and Physics* (CRC Press, Boca Raton, 2004), 84th edn.

[161] D. C. Cronemeyer, Phys. Rev. **113**, 1222–1226 (1959).

CURRICULUM VITAE

Name: Valter Kiisk
Date and place of birth: 17. august 1977, Rakvere
Nationality: Estonian
Citizenship: Estonian
Marital status: single
Occupation: PhD student at the Department of Physics of the University of Tartu
Phone: +3727428882 (at work), +37255964683 (cell phone)
E-mail: kiisk@ut.ee

Education

1985 – 1996	Rakvere Gymnasium
1996 – 2000	University of Tartu (Department of Physics). Diploma: June 27, 2000.
2000 – 2002	University of Tartu (Department of Physics). M. Sc. in physics: June 10, 2002.
2002 – 2006	PhD student at the University of Tartu (solid state physics)

Language skills

Estonian (mother tongue), English (good), Russian (elementary knowledge).

Professional employment

1997 – 2004	Institute of Physics of the Univrsity of Tartu, technician
2004 – 2006	Institute of Physics of the Univrsity of Tartu, engineer

CURRICULUM VITAE

Nimi: Valter Kiisk
Sünniaeg ja -koht: 17. august 1977, Rakvere
Rahvus: eestlane
Kodakondsus: Eesti
Perekonnaseis: vallaline
Praegune töökoht, amet: Tartu Ülikooli Füüsika Instituut, doktorant
Telefon: 7428882 (tööl), 55964683 (mobiil)
E-post: `kiisk@ut.ee`

Haridustee

1985 – 1996	Rakvere Gümnaasium
1996 – 2000	Tartu Ülikool (füüsika osakond), lõpetanud füüsika eriala 27. juunil 2000
2000 – 2002	Tartu Ülikool (füüsika osakond), magistrikraad tahkisefüüsikas 10. juunil 2002
2002 – 2006	Tartu Ülikooli doktorant (tahkisefüüsika)

Keelteoskus

Eesti (emakeel), inglise (hea), vene (algteadmised).

Erialane teenistuskäik

1997 – 2004	Tartu Ülikooli Füüsika Instituut, laborant
2004 – 2006	Tartu Ülikooli Füüsika Instituut, insener